RESEARCH ARTICLE

Key Points:
- Introduce new transformation scheme mapping interferometric TEC gradient data onto magnetic shell tangent plane
- Physically meaningful coordinates enable decomposition of field-transverse and field-aligned behavior
- Demonstrate technique for measuring magnetic inclination from TEC data and verify geomagnetic alignment of irregularities observed by MWA

Supporting Information:
- Supporting Information S1
- Movie S1

Correspondence to:
S. T. Loi,
stl36@cam.ac.uk

A new angle for probing field-aligned irregularities with the Murchison Widefield Array

Shyeh Tjing Loi[1,2,3], Tara Murphy[1,2], Iver H. Cairns[4], Cathryn M. Trott[2,5], Natasha Hurley-Walker[5], Lu Feng[6], Paul J. Hancock[2,5], and David L. Kaplan[7]

[1]Sydney Institute for Astronomy, School of Physics, University of Sydney, Sydney, New South Wales, Australia, [2]ARC Centre of Excellence for All-sky Astrophysics, Sydney, New South Wales, Australia, [3]Department of Applied Mathematics and Theoretical Physics, Centre for Mathematical Sciences, University of Cambridge, Cambridge, UK, [4]School of Physics, University of Sydney, Sydney, New South Wales, Australia, [5]International Centre for Radio Astronomy Research, Curtin University, Bentley, Western Australia, Australia, [6]Kavli Institute for Astrophysics and Space Research, Massachusetts Institute of Technology, Cambridge, Massachusetts, USA, [7]Department of Physics, University of Wisconsin-Milwaukee, Milwaukee, Wisconsin, USA

Abstract Electron density irregularities in the ionosphere are known to be magnetically anisotropic, preferentially elongated along the lines of force. While many studies of their morphology have been undertaken by topside sounding and whistler measurements, it is only recently that detailed regional-scale reconstructions have become possible, enabled by the advent of widefield radio telescopes. Here we present a new approach for visualizing and studying field-aligned irregularities (FAIs), which involves transforming interferometric measurements of total electron content gradients onto a magnetic shell tangent plane. This removes the perspective distortion associated with the oblique viewing angle of the irregularities from the ground, facilitating the decomposition of dynamics along and across magnetic field lines. We apply this transformation to the data set of Loi et al. (2015a), obtained on 15 October 2013 by the Murchison Widefield Array (MWA) radio telescope and displaying prominent FAIs. We study these FAIs in the new reference frame, quantifying field-aligned and field-transverse behavior, examining time and altitude dependencies, and extending the analysis to FAIs on subarray scales. We show that the inclination of the plane can be derived solely from the data and verify that the best fit value is consistent with the known magnetic inclination. The ability of the model to concentrate the fluctuations along a single spatial direction may find practical application to future calibration strategies for widefield interferometry, by providing a compact representation of FAI-induced distortions.

1. Introduction

1.1. Plasma Density Irregularities

The Earth's plasma environment abounds with density irregularities, on scales ranging from those of neutral atmosphere waves (100–1000 km) down to ion and electron gyroradii (0.1–1 m) [*Yeh and Liu*, 1974; *Booker*, 1979; *Fung et al.*, 2000; *Akmaev*, 2011; *Wang et al.*, 2011; *Nicolls et al.*, 2014]. They tend to be elongated along the geomagnetic field lines owing to large electron mobilities in this direction and are broadly referred to as field-aligned irregularities (FAIs) [e.g., *Sonwalkar*, 2006; *Makela and Otsuka*, 2012]. Acoustic-gravity waves (AGWs), which couple to charged species via collisions, are believed to be the source of energy driving the formation of smaller-scale density structures, for example, via the spatial resonance mechanism [*Whitehead*, 1971; *Klostermeyer*, 1978] or upon passage through a critical layer [*Booker and Bretherton*, 1967; *Staquet and Sommeria*, 2002], with further cascades possible through various plasma instabilities and nonlinear processes [*Perkins*, 1973; *Fejer and Kelley*, 1980; *Maruyama*, 1990; *Nicolls and Kelley*, 2005]. Observational evidence for the association between AGWs and FAIs was recently presented by *Sun et al.* [2015] and *Loi et al.* [2016].

FAIs of suitable dimensions and density contrasts are capable of ducting and guiding VLF to HF radio waves, a property that enabled their initial discovery [*Storey*, 1953] and subsequent investigations [*Calvert and Warnock*, 1969; *Angerami*, 1970; *Singh et al.*, 1998; *Darrouzet et al.*, 2009]. Studies of their morphology have mostly relied on theoretical knowledge about electromagnetic (EM) wave trapping and guidance by plasma density structures [*Smith et al.*, 1960; *Calvert*, 1995], aided by ray tracing calculations to interpret received signal patterns [*Haselgrove*, 1955; *Smith*, 1961; *Dyson*, 1967; *Hayakawa and Tanaka*, 1978;

Fung and Green, 2005; *Kulkarni et al.*, 2008]. Sheet-like structures extended in the east-west direction have been posited as one interpretation of topside sounder data [*Muldrew*, 1963; *Dyson*, 1967], possibly occurring in uniformly spaced onion-like layers [*Gross and Muldrew*, 1984].

Numerical studies suggest that tubular structures can also be effective waveguides [*Smith*, 1961; *Platt and Dyson*, 1989]. The existence of tubular structures with inferred widths of 10–100 km has been established through satellite in situ measurements [*Angerami*, 1970; *Sonwalkar et al.*, 1994; *Décréau et al.*, 2005], satellite remote sensing [*Fung et al.*, 2003; *Darrouzet et al.*, 2009; *Woodroffe et al.*, 2013], ground-based whistler spectrograms [*Hayakawa and Tanaka*, 1978; *Singh et al.*, 1998; *Altaf and Ahmad*, 2013], and ground-based radio interferometric arrays [*Jacobson and Erickson*, 1993; *Hoogeveen and Jacobson*, 1997a; *Helmboldt and Intema*, 2012]. Recent interferometric observations support the idea that tubular FAIs may in some instances be confined to a narrow sheet-like layer on a single magnetic shell [*Loi et al.*, 2015a, 2015b]. Subtler details such as field-aligned density profiles have been measured through VLF whistler observations [*Carpenter and Smith*, 1964; *Lichtenberger*, 2009; *Lichtenberger et al.*, 2013], ULF field-line resonances [*Menk et al.*, 1999], and topside sounding [*Dyson and Benson*, 1978; *Tu et al.*, 2006].

The growth and decay rates of FAIs depend on many factors, including the electrical conductivity, electric and magnetic fields, ambient densities and density gradients, collisional frequencies, and drift velocities [*Farley*, 1963; *Fejer and Kelley*, 1980; *Ossakow*, 1981; *Sojka et al.*, 1998; *Fejer et al.*, 1999]. Numerical and experimental results suggest that growth due to various instabilities may occur on timescales of minutes to tens of minutes [*Park and Helliwell*, 1971; *Sojka et al.*, 1998; *Carter et al.*, 2014] and decay by cross-field diffusion on timescales of hours to days [*Thomson*, 1978; *Singh and Singh*, 1999; *Singh et al.*, 2013].

1.2. Radio Interferometry

Many radio telescopes are interferometric arrays that measure the phase difference of incoming EM waves between pairs of receivers [*Thompson et al.*, 2001]. Since the refractive index of a plasma is electron density dependent, interferometers can detect density gradients through phase fluctuations. In an interferometric image, these manifest as shifts in the angular position of a radio source and/or broadening of the angular extent of a source and may also be accompanied by intensity fluctuations [*Hamaker*, 1978; *Bougeret*, 1981; *Spoelstra and Kelder*, 1984; *Jacobson and Erickson*, 1992a; *Cotton et al.*, 2004; *Cohen and Röttgering*, 2009]. It is in the interest of those using radio telescopes for astronomical observations to model and subtract these distortions from (i.e., calibrate) the data. The development of ionospheric calibration strategies for newly emergent widefield interferometers operating in the VHF band is an ongoing challenge, with a variety of approaches being trialed [*Cotton et al.*, 2004; *Intema et al.*, 2009; *Arora et al.*, 2015; *van Weeren et al.*, 2016].

Bulk angular shifts are caused by density gradients whose scale lengths greatly exceed the physical size of the interferometric array, forming a wedge that collectively tilts the wavefront normals arriving at all baselines [*Thompson et al.*, 2001]. The associated displacement $\Delta\theta$ (in radians) is directly proportional to the transverse TEC gradient $\nabla_\perp \mathrm{TEC}$ (in el m^{-3}) and inversely proportional to the observing frequency ν (in Hz) according to

$$\Delta\theta \approx -\frac{40.3}{\nu^2}\nabla_\perp \mathrm{TEC} . \tag{1}$$

Angular broadening can be conceived as the result of superposing multiple wavefront normals, which might occur if irregularity scale sizes fall below the size of the array (different baselines experience different phase deviations), or if integration times exceed the timescale of variation in the plasma along the line of sight [*Spoelstra and Kelder*, 1984; *Lonsdale*, 2005; *Kassim et al.*, 2007]. Intensity variations can arise from focusing and defocusing of the incoming rays, becoming extreme (modulation indices of order unity) in the diffraction-dominated limit [*Meyer-Vernet*, 1980; *Booker and Majidiahi*, 1981; *Spoelstra*, 1985]. These effects are illustrated in the cartoon in Figure 1. Note that a perfectly uniform TEC screen cannot be detected by an interferometer, since it is only the phase difference and not the absolute phase that is measured on a baseline (it is in principle possible to measure the absolute TEC through Faraday rotation, but the precision of this is lower).

To perform the phase measurements the telescope must have a source of back-illuminating radio waves. These can be naturally occurring, e.g., solar active regions [*Bougeret*, 1981; *Mercier*, 1986] or cosmic radio sources [*Hamaker*, 1978; *Jacobson and Erickson*, 1993; *Spoelstra*, 1997; *Helmboldt*, 2014; *Loi et al.*, 2015b], or of man-made origin such as satellite beacons [*van Velthoven*, 1990; *Jacobson et al.*, 1996; *Hoogeveen and Jacobson*, 1997b]. Celestial sources of radio emission, though faint in comparison to solar or man-made
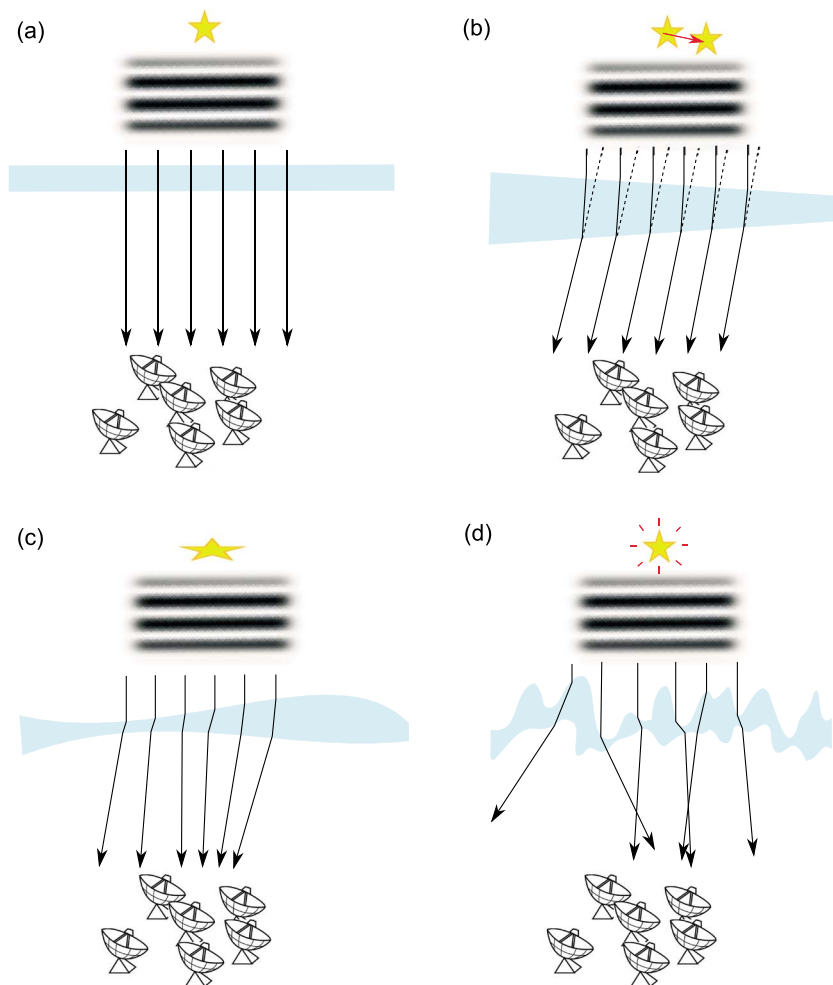
Figure 1. A cartoon illustration of the effects of phase distortions induced by the ionosphere. (a) In the case of a smooth ionosphere, there is no change in the differential phase. (b) In the linearly varying case, a simple angular shift results. (c) Higher-order spatial variations cause shape distortion. (d) For sufficiently small irregularities a nonlinear diffractive regime is reached, resulting in scintillation.

sources, are stable in output and detectable at a rate of about one per square degree on the sky, for a confusion-limited interferometer with 2 arc min angular resolution operating in the VHF band. The exploitation of their abundance to construct spatially detailed, regional-scale TEC gradient maps has been made possible by the recent development of sensitive, widefield radio telescopes [*Loi et al.*, 2015b, 2015c].

Detections of tubular FAIs by interferometric arrays were previously made using the Westerbork Radio Synthesis Telescope [*van Velthoven*, 1990], the Very Large Array (VLA) [*Jacobson and Erickson*, 1992b, 1993; *Hoogeveen and Jacobson*, 1997a; *Helmboldt et al.*, 2012a], and the Los Alamos interferometer [*Jacobson et al.*, 1996; *Hoogeveen and Jacobson*, 1997b]. Increasingly sophisticated analysis methods for the VLA, designed to cope with its sparse spatial sampling, have been under recent development [*Cohen and Röttgering*, 2009; *Coker et al.*, 2009; *Helmboldt et al.*, 2012b; *Helmboldt and Intema*, 2012; *Helmboldt*, 2014]. The sparseness with which traditional interferometers sample the TEC distribution is contrasted by the breadth and detail achieved by new generation instruments such as the Murchison Widefield Array (MWA) [*Lonsdale et al.*, 2009; *Bowman et al.*, 2013; *Tingay et al.*, 2013], which permit rich visualizations of FAIs and traveling disturbances over wide fields of view [*Loi et al.*, 2015a, 2016]. Tubular FAIs have been observed in half or more of nighttime MWA data, to varying degrees of prominence [*Loi et al.*, 2015b]. Their high occurrence rate over the site of the MWA suggests that they must be accounted for if a thorough calibration of ionospheric effects is desired. However, their steep inclination with respect to the ground implies that constant-altitude screen models might be unsuitable and that a more flexible model is needed to capture their properties.

1.3. This Work

We present a new method for visualizing and studying FAIs, designed for widefield interferometers, that involves mapping TEC gradients measured from radio synthesis images onto a plane tangent to a magnetic shell. This transformation removes the perspective distortion associated with inclined magnetic field lines, providing a physically meaningful reference frame in which to inspect their properties. We apply this technique to the data set previously analyzed by *Loi et al.* [2015a], known to exhibit prominent FAIs. We also extend the analysis to subarray scales, something which has not been previously done with MWA data, by examining angular broadening effects.

The paper is structured as follows. In section 2 we introduce the model. In section 3 we introduce the MWA observations, explain the analysis approaches for large- and small-scale irregularities, and demonstrate how the best fit inclination may be obtained. Our results are presented in sections 4 and 5 for large- and small-scale irregularities, respectively. We conclude in section 6.

2. The Inclined Plane Model

The quantity measured by an interferometer through the angular displacement of an unresolved (point-like) radio source is $\nabla_\perp$TEC, the gradient of the TEC transverse to the line of sight to the source. Because it involves an absolute reference length scale (the spacing between receivers), this gradient is independent of the distance to the irregularities causing the phase perturbation. It is a two-dimensional vector, lying in the plane perpendicular to the line of sight. In addition, the angular position of the origin of this vector is known, given by the angular position of the source, also a two-component vector. For a celestial source, this is usually specified in terms of the right ascension α and declination δ (not to be confused with magnetic declination), which are coordinates fixed with respect to the celestial sphere. There are in total thus four independent input quantities: α, δ, ∂_αTEC, and ∂_δTEC, where the partial derivative shorthand ∂_X denotes the gradient along direction X.

Geometric arguments presented by *Loi et al.* [2015a] and *Loi et al.* [2015b] indicate that FAIs observed over the MWA site are often confined to a narrow layer, i.e., small L value [*McIlwain*, 1961] range, though this value of L may differ between observations. This motivates the introduction of a model that maps the four observables onto such a surface. In this work, we consider the lowest-order approximation to achieve this, namely, an inclined 2-D plane (i.e., a flat screen) tangential to the L shell on which the irregularities reside. We assume that all phase perturbations are taken up by this screen, whose thickness is negligible. Clearly this is only valid locally since the curvature of field lines is neglected. Given that the scale of curvature is of order the radius of the Earth (several thousand kilometers) and that the measurements probe a region several hundred kilometers across, we expect this approximation to be reasonable.

Although a general 2-D plane in 3-D space requires three parameters for a full description, one of these can be eliminated by enforcing the east-west component of the normal vector to be zero (N.B. at the site of the MWA, geomagnetic and geographic east-west coincide to within a degree and so their difference can be conveniently neglected; see Appendix A for how to handle the more general case). This is equivalent to assuming axisymmetry of the Earth's magnetic field, a good approximation for the inner magnetosphere where the field is close to being dipolar. This leaves two independent parameters, which we define to be h, the altitude of the plane at the point directly above the MWA, and i, the inclination angle (measured positive for a plane sloping upward toward the north). These two quantities are illustrated in Figure 2. Suitable values for h and i can in fact be derived solely from the data without any knowledge of the geomagnetic field: h can be estimated via a parallax technique [*Loi et al.*, 2015a] and i can be optimized by demanding that it maximizes the "parallelness" of resultant features (quantitative details in section 3.4).

To describe position on the plane itself, we define an orthogonal basis $(\hat{\xi}, \hat{\eta})$ where the $\hat{\xi}$ axis points west and the $\hat{\eta}$ axis points north (see Figure 2). The equations for how to map celestial coordinates (α, δ) to screen coordinates (ξ, η), which make use of the intermediary (β, γ) system introduced by *Loi et al.* [2015b], are given in Appendix A. Note that the (ξ, η) coordinates are not geographically absolute but are defined with respect to the observing location, with $\xi = \eta = 0$ corresponding to the observer's zenith.

As explained earlier in section 1.2, an interferometer is insensitive to the zeroth-order (i.e., constant offset) component of the TEC distribution. This implies that if density irregularities are confined to a thin layer bounded above and below by smooth plasma, then this is observationally equivalent to a thin plasma screen
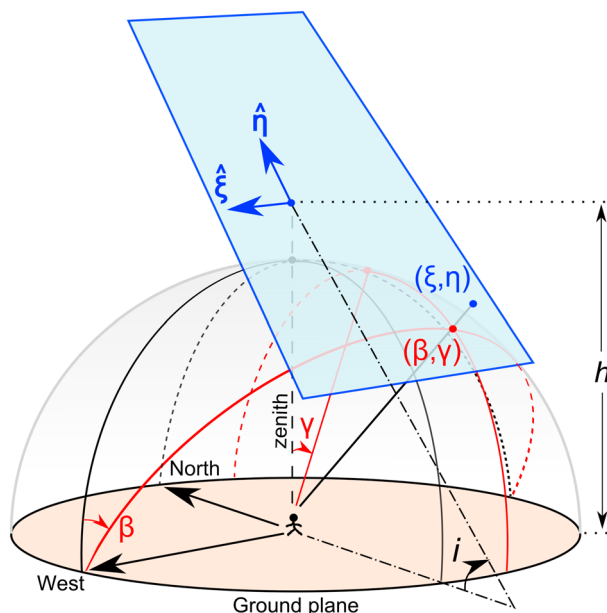
Figure 2. Diagram showing the geometry of the model and how the (β, γ) and (ξ, η) coordinate systems are defined with respect to the ground observer. Cardinal directions are as marked. The (β, γ) coordinates, shown in red, are angular coordinates for an imaginary sphere centered on the observer (note that the finite radius of the sphere as drawn in this diagram is solely for visualization purposes and otherwise has no meaning). These are the same (β, γ) coordinates as described in *Loi et al.* [2015b]. The (ξ, η) coordinates, shown in blue, are Cartesian coordinates describing position on the inclined plane. The origin of this system is defined to be the point on the plane directly overhead of the observer. The two parameters describing the plane, which are the inclination angle i and zenith altitude h, are defined as shown. In the current model the normal vector to the plane is assumed to have zero (cardinal) east-west component.

bounded above and below by vacuum. In the context of our model, we thus find it natural to associate a surface density rather than a column density to points on the screen (although given that the two have equivalent units, the difference is mainly conceptual). We denote this surface density by Σ, a scalar function of ξ and η. The gradient of Σ with respect to the screen can be determined by a suitable transformation of the $\nabla_\perp$TEC vector. For our simple model, it is possible to obtain explicit expressions for $\partial_\xi \Sigma$ and $\partial_\eta \Sigma$ in terms of the four input quantities. These and further details are contained in Appendix A.

The effect of the transformation from angular to screen coordinates for an arbitrary snapshot from the data set of *Loi et al.* [2015a] is demonstrated in Figure 3. The coordinate system in Figure 3a is the one which has been used for visualization in previous MWA work and corresponds to the view one might have looking up at the structures from the ground (see *Loi et al.* [2015b] for a qualitative overview and Appendix A of the current work for quantitative details). On the other hand, Figure 3 is the view one might have from a vantage point looking "face on" at the surface on which the irregularities reside. We can visually identify two consequences of the transformation: (i) there is an "unskewing" of apparently convergent features into a much more parallel configuration and (ii) the gradient vectors turn out to be nearly parallel to the ξ axis. While the first property is to be expected from the way in which i was chosen (to maximize the parallelness of features; details in section 3.4), the second property is an independent verification that the model is physically reasonable (larger density gradients can be sustained across than along field lines).

3. Methods

3.1. Instrument, Observations, and Data

The MWA telescope is an interferometric array sited at a midlatitude location in Western Australia, at a geographic latitude of 26.7°S and a geomagnetic latitude of 38.6°S ($L = 1.6$). It operates at frequencies between 80 and 300 MHz (in the VHF band). Its 128 receiving elements (tiles) are spread over a total region about 3 km wide on the ground but are centrally condensed, with most (112 out of 128) tiles lying within 0.75 km of the core. The MWA therefore behaves as a point detector for structures greatly exceeding 1 km and a distributed array for structures on much smaller scales. The instantaneous angular field of view (FOV) of the MWA is 30°, subtending a physical distance of about 300 km at 600 km altitude.
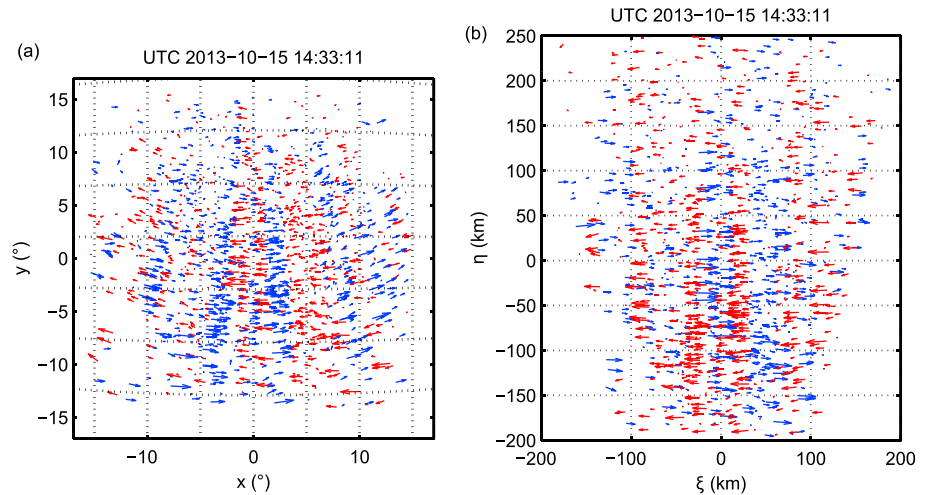
Figure 3. A comparison of the electron density gradient vector field from a particular snapshot computed with respect to (a) a Sanson-Flamsteed projection of the (β, γ) coordinates and (b) the new (ξ, η) coordinates. The parameters used are $h = 570$ km and $i = 59°$. Note that in both cases the sky is into the page, so that the vertical axis points north and the horizontal axis points west. Horizontal and vertical dotted lines in Figure 3a correspond to lines of constant β and γ, while those in Figure 3b correspond to lines of constant η and ξ, respectively. In Figure 3a, the relationship between (x, y) and (β, γ) is given by *Loi et al.* [2015b, equation (3)]. It is to be noted that the (x, y) and (β, γ) systems nearly coincide (the dotted lines are very close to being x and y gridlines). Arrows lengths are directly proportional to the magnitude of the gradient vector and scaled for clarity, such that a 1° long arrow in Figure 3a represents a gradient of 2.9×10^{14} el m^{-2} km^{-1}, while a 10 km long arrow in Figure 3b represents a gradient of 1.4×10^{14} el m^{-2} km^{-1}. Blue and red colors are an aid to visualization and denote arrows with positive and negative horizontal components, respectively.

The data set considered in this paper is the same as the one discussed by *Loi et al.* [2015a]. It was obtained during mildy disturbed geomagnetic conditions ($K_p = 2$) within the recovery phase of a moderate (minimum $Dst = -45$ nT, 24 h maximum $K_p = 4$) geomagnetic storm on 15 October 2013. The data were recorded at 183 MHz (30.72 MHz instantaneous bandwidth) over a 1.5 h long interval between 1346 and 1517 UTC (2146–2317 Australian Western Standard Time). Prominent FAIs are present over the whole FOV during this period. Their characteristic altitude was established by *Loi et al.* [2015a] to be 570 ± 40 km.

The interval comprises 46 blocks of data spaced by 2 min and recorded over 112 s each. However, the interferometric visibilities (i.e., complex voltages) were in fact captured at 0.5 s time resolution. While most of the analysis here uses images formed by integrating over the 112 s of data in each 2 min block, a portion of this work (section 5) makes use of images formed at a much higher cadence of 4 s. This allows short-term dynamics to be elucidated at the expense of diminished image sensitivity.

3.2. Probing Large-Scale Structure

As discussed earlier, the size of the array determines how phase fluctuations of various scales manifest in the data. Hereafter we define "large scale" to mean structures larger than the diameter of the MWA ("super-MWA" scales). Practically speaking, these are the structures that can be probed through the displacements they induce in the positions of unresolved radio sources. The method for extracting these angular displacements in the current work is identical to that described in previous MWA work [*Loi et al.*, 2015a, 2015b, 2015c, 2016], to which we refer the reader for further details.

Briefly, this involved first identifying candidate radio sources by searching for intensity maxima in the images above a given noise threshold, cross matching them with a published astronomical database (here the National Radio Astronomy Observatory VLA Sky Survey, NVSS) [*Condon et al.*, 1998] and retaining only those with counterparts. The displacement vector $\Delta\theta$ associated with an NVSS source appearing in a certain snapshot was taken to be the difference between its position measured in that snapshot and its time-averaged position. The $\Delta\theta(\alpha, \delta)$ vectors were then mapped to $\nabla\Sigma(\xi, \eta)$ vectors by the transformation steps described in section 2 and Appendix A. Results pertaining to large-scale structure are discussed in section 4.

3.3. Probing Small-Scale Structure

We define "small scale" here to refer to structures on sub-MWA scales. These fluctuations are responsible for the apparent broadening of otherwise unresolved radio sources; one can envisage this as arising from the

simultaneous arrival of wavefronts with different orientations over different parts of the array. The spread of angular offset vectors causes the source to appear blurred. The amount and orientation of the broadening relate to the spread in wavefront orientations, which in turn arises from the spread in $\nabla_\perp$TEC on subarray scales. The "broadening vector" (defined in more detail below) associated with this process therefore obeys the same transformation rules as the $\nabla_\perp$TEC vectors measured through bulk angular displacements.

To probe structures in the sub-MWA regime we made use of images formed at 4 s rather than 2 min cadence, to minimize the size of the region sampled toward each source. The drift of celestial sight lines through the screen occurs at a speed of ~40 m s^{-1} at 600 km altitude, meaning that each patch of sight lines sweeps out an area roughly 3 times larger in a 2 min compared to a 4 s image, assuming an effective MWA diameter of 1.5 km (4.8×1.5 km^2 versus 1.7×1.5 km^2).

The software package used for automated source extraction (AEGEAN) [*Hancock et al.*, 2012] operates by fitting 2-D elliptical Gaussians to intensity maxima. Besides the best fit coordinates of the center of the Gaussian, AEGEAN also reports the major axis b_{maj}, minor axis b_{min}, and position angle p (measured east of north). In the absence of any scatter broadening, the width of a source in an image is given by the width of the synthesized beam (response function), which for the MWA at 183 MHz is about 2 arc min. The MWA synthesized beam is approximately a circular Gaussian, but the exact shape and size can vary over time if certain tiles/baselines are temporarily excised due to interference or hardware malfunctions (largely an automated process). The broadening due to finite angular resolution is distinct from scatter broadening.

Our approach to isolating the scatter broadening contribution was to take the quadrature difference between the major and minor axes fitted for the Gaussian, which we call the *broadening width*. This leads to our definition of the *broadening vector* **b** as the vector oriented parallel to the major axis whose associated magnitude is the broadening width:

$$\mathbf{b} = \pm\sqrt{b_{maj}^2 - b_{min}^2}\left(\frac{\sin p}{\cos \delta}, \cos p\right), \tag{2}$$

given with respect to the (α, δ) basis. The $\pm$ sign reflects the fact that **b** is a spin-2 vector (since the orientation of the major axis is only defined modulo 180°). The broadening vectors take the role of the angular displacement vectors $\Delta\theta$ described in section 2 and Appendix A as the measure of TEC fluctuation. We subjected the **b** vectors to an identical sequence of transformations to obtain the sub-MWA version of "$\nabla\Sigma$," which is more closely related to the second spatial derivative of Σ.

Note that the manner in which we have quantified the scatter broadening contribution assumes that the broadening occurs primarily along a selected direction and is therefore a conservative lower bound on the actual amount of broadening. Physically we expect density irregularities below ~1 km scales to be highly anisotropic, because these scales are less than the mean free path of neutrals in the thermosphere (several kilometers) [*Jacchia*, 1977] and shaped by magnetic forces rather than collisions. We thus expect small-scale irregularities to be strongly field aligned, producing broadening in the direction perpendicular to their elongation (cf. a diffraction grating). Indeed, the data exhibit both a larger fraction of sources broadened along ξ and a larger average broadening width in this direction, compared to η (Figure 4).

Referring to the average broadening width for sources whose **b** vectors lie within 15° of the ξ and η axes as w_ξ and w_η, respectively, we also see from Figure 4 that w_ξ grows with time. This is closely reminiscent of the growth of the larger-scale structures apparent in *Loi et al.* [2015a, Figure 3c]. In contrast, w_η exhibits no such growth. Noting that w_η turns out to be comparable to the error on b_{maj} and b_{min} quoted by AEGEAN, we can regard this as a measure of the noise floor. Subtracting this in quadrature from w_ξ, we thus arrive at the following conservative estimate of the spread in $\nabla\Sigma$ due to small-scale FAIs:

$$\sigma(\nabla\Sigma) = \frac{1}{2}\sqrt{w_\xi^2 - w_\eta^2}. \tag{3}$$

The factor of 1/2 reflects the fact that w_ξ and w_η are major axis-related quantities, while σ is a root-mean-square (RMS) quantity, which is related to the semimajor axis of a Gaussian distribution. Unit conversion factors have been omitted for clarity. The results for small-scale structure are presented in section 5.

3.4. Choosing the Height and Inclination
In section 2 we introduced the two free parameters h and i, which are inputs to the model and illustrated in Figure 2. The best fit average height of the irregularities in the 15 October 2013 data set was determined
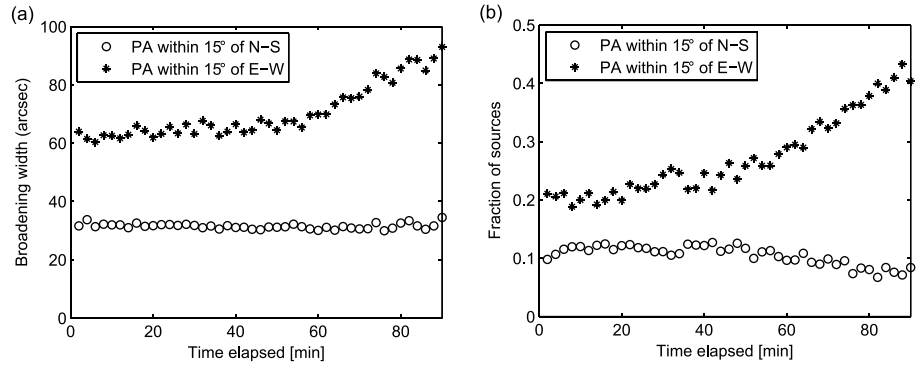
Figure 4. (a) The broadening width (quadrature difference of major and minor axes) as a function of time, for sources whose position angles are aligned with the ξ and η axes. The alignment criterion has been taken to be a position angle within 15° of the respective axis. (b) The fractions of sources selected by these restrictions on orientation, as a function of time. This analysis makes use of the 4 s cadence data to minimize the spatial extent of the region sampled by the drifting sources. Only sources of signal-to-noise ratio greater than 10 have been included.

previously by *Loi et al.* [2015a] to be 570 ± 40 km, and so the value of h we adopt in this work is $h = 570$ km. Fortunately, the uncertainty in this value only affects the physical scale inferred for the irregularities, and not the orientation or the magnitude of $\nabla\Sigma$. This can be seen directly from equations (A3) and (A4), which are independent of h.

The value of i can be set to be the magnetic inclination, which is known from geomagnetic reference models [e.g., *Geoscience Australia*, 2010]. However, this value can be directly fitted using MWA data without any prior knowledge of the magnetic field, serving as a useful quantitative cross check of the assumption that the irregularities are field aligned. We did this by finding the i that maximized the parallelness of features in the resulting $\nabla\Sigma$ distribution. In more quantitative terms, we made use of the power spectrum technique developed by *Loi et al.* [2015b] applied to the new $\nabla\Sigma(\xi,\eta)$ vector field to obtain the total power of fluctuations with $k_\eta = 0$, where k_η denotes spatial frequency along the η direction. These are the fluctuation modes whose phase fronts are parallel to the η axis. In the notation of *Loi et al.* [2015b] (sections 3.3 and 3.4), but replacing $x \to \xi, y \to \eta, \Delta x \to \partial_\xi\Sigma$, and $\Delta y \to \partial_\eta\Sigma$, the optimization problem can be stated quantitatively as the desire to find the i maximizing

$$F(i) = \frac{V}{N_\xi N_t} \sum_{\ell=1}^{N_\xi} \sum_{n=1}^{N_t} \left[\mathcal{P}_{\ell 1n}(0°) + \mathcal{P}_{\ell 1n}(90°) \right] . \qquad (4)$$

This is the discrete version of the sum of the integrals of the power spectral density over k_ξ and ω for the two scalar fields $\partial_\xi\Sigma$ and $\partial_\eta\Sigma$ (corresponding to the arguments of 0° and 90° in the above expression, respectively). The units of $\mathcal{P}$ in the current work are el^2 m^{-4} s. We gridded the data at a resolution of 2 km.
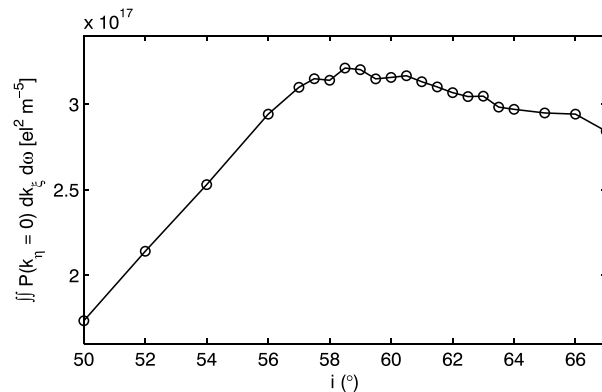

Figure 5. The degree of "ξ parallelness" of features, measured through a spatial Fourier transform (details in text), as a function of the plane inclination i. This maximizes at around $i = 59°$, which is consistent with the known inclination of geomagnetic field lines within the MWA FOV (see text for discussion). A value of $i = 59°$ has been adopted for all analyses in this work.
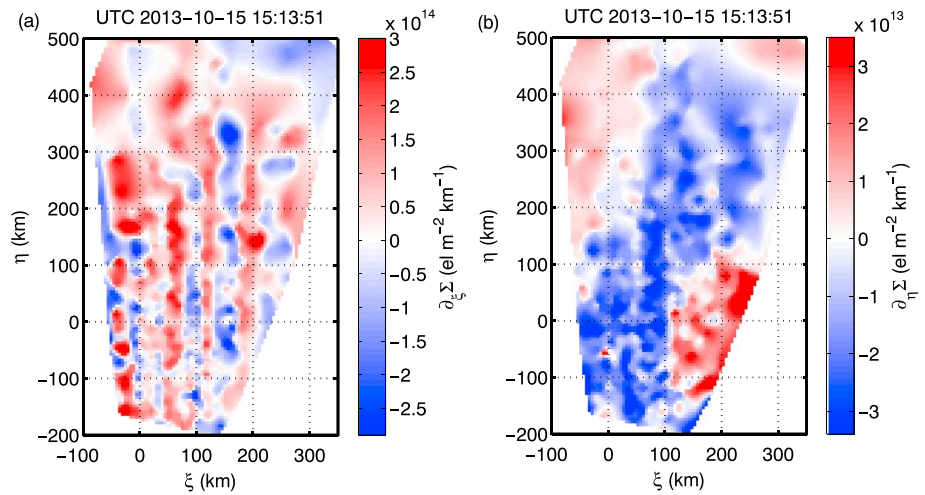
Figure 6. The (a) ξ and (b) η components of the $\nabla\Sigma$ vector field, for a particular snapshot. Red and blue correspond to positive and negative gradients, and white corresponds either to near-zero values or regions outside the FOV (i.e., unmeasured values). These have been generated by first forming a natural neighbor interpolant over the data, resampling over a 5 km uniform grid and then smoothing the result with a 3×3 box median filter. The shorthand $\partial_X \equiv \partial/\partial X$ has been used to denote a partial derivative. See Movie S1 for an animation of the full data set.

The quantity F is plotted versus i in Figure 5. This exhibits a maximum near $i = (59\pm1)°$. Although this seems to differ slightly from the zenith value of the magnetic inclination at a height of 570 km, which is 60.3° [*Geoscience Australia*, 2010], this can be explained by noticing that the north-south physical span of the plane within the FOV is in fact biased toward the north (by ~100 km, as can be seen in Figure 6). Since the magnetic inclination is shallower toward the north, the average inclination over the FOV should be slightly smaller than the zenith value: at 50 ($=100\cos 60°$) km north of the MWA it is 59.7°, and incorporating in addition the curvature of the Earth away from an observer by ~0.5° every 50 km, it is within expectation that the best fit value of i lies closer to 59° than 60°. In all subsequent analyses we adopted a value of $i = 59°$. Our results change very little with variations of this value by ~1°.

As a final comment in this section, we note that the near constancy of the magnetic inclination along the line through zenith precludes the possibility of inferring h through a fit to i. This has previously been done for similar structures (using other interferometers) when lines of sight have been suitably oblique [*Jacobson et al.*, 1996; *Hoogeveen and Jacobson*, 1997a, 1997b]. However, the advantage here is that we have been able to quantitatively verify that the irregularities are indeed consistent with field alignment (to within ~1°), whereas the previous works held this as a model assumption.

4. Super-MWA Structures

4.1. Morphology

Figure 6 shows the spatial distributions of $\partial_\xi\Sigma$ and $\partial_\eta\Sigma$, the two orthogonal components of the $\nabla\Sigma$ vector field, for a representative snapshot from the *Loi et al.* [2015a] data set. Movie S1 (see supporting information) shows the time evolution for the whole data set. For the purposes of visualization, the discretely sampled data have been interpolated onto a uniform 5 km grid. This spacing is about half the average pierce-point separation. A representative distribution of the actual pierce points is shown in Figure 3b, where one arrow corresponds to one pierce point. The sampling becomes sparser toward the north (higher altitudes) because the same solid angle subtends a greater physical area at a larger distance.

Figures 6a and 6b correspond to the field-transverse (i.e., direction in the plane perpendicular to the magnetic field) and field-aligned density gradients, respectively. We see that vertical (i.e., η parallel) striations are prominent in the field-transverse component of $\nabla\Sigma$, but not the field-aligned component. Typical length scales are about an order of magnitude smaller in the field-transverse than field-aligned directions. This is unsurprising because the Lorentz force acts perpendicular to the magnetic field lines and can only sustain against diffusion in this direction. Gradients along the η direction would be caused by other effects, such as modulations by hydrodynamic or MHD waves [*Poole et al.*, 1988; *Kazimirovsky et al.*, 2003; *Menk et al.*, 2007;
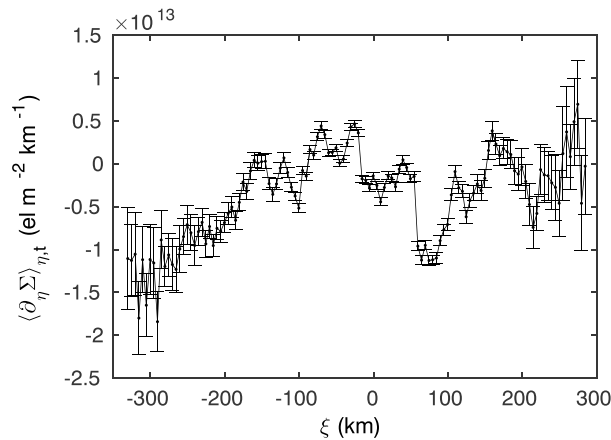
Figure 7. The average (over time and η) η gradient, as a function of ξ. Physically, this is the field-aligned density gradient of each flux tube as a function of its longitudinal position. Points have been binned in 5 km intervals along the ξ direction, and a minimum of 10 points in a bin is required for the bin to be shown on the plot. Error bars represent the standard error (standard deviation divided by the square root of the number of points) for each bin.

Fritts and Vadas, 2008; *Waters and Cox*, 2009]. This illustrates the usefulness of the (ξ, η) basis in allowing us to decompose structures shaped by different physical processes.

Also apparent from Figure 6 is the difference in magnitudes of field-transverse and field-aligned gradients. Field-transverse gradients are about an order of magnitude steeper than field-aligned gradients, which is similarly consistent with physical expectations. In Movie S1 it can be seen that both components of $\nabla\Sigma$ increase in magnitude over time, indicating that the observation interval captured a period of growth. We discuss this further in section 4.5.

4.2. Field-Aligned Density Gradients

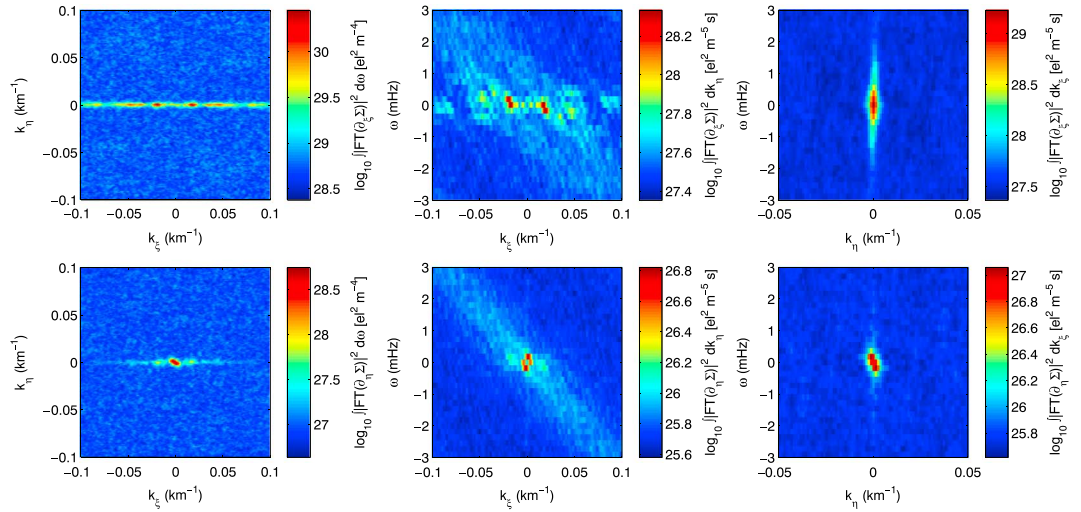Under diffusive (i.e., hydrostatic) equilibrium, one expects Σ to decrease with altitude ($\partial_\eta\Sigma < 0$) along each flux tube. However, we can see from Figure 6 and Movie S1 that $\partial_\eta\Sigma$ exhibits variations along η on scales of several hundred kilometers and that this can apparently take both positive and negative values (red and blue hues, respectively). However, we have measured angular offsets not with respect to an absolute reference but rather the time-averaged position, which subtracts away fluctuations that are stationary with respect to the celestial sphere. (The choice to use the time-averaged position as the reference, as has been done in all previous MWA works, stems from the inability to obtain an accurate absolute reference for this analysis; see *Loi et al.* [2015c], section 2.3 for details). This implies that the $\partial_\eta\Sigma$ values are not absolute but should rather be interpreted as fluctuations about some unmeasured global mean.

Despite this limitation, there are still useful conclusions that can be drawn from the data. The rotation of the Earth causes each pierce point to drift roughly east-west (i.e., in the ξ direction) through the screen, and so a large fraction, particularly in the central ξ range of the area scanned, eventually drift across (sample) each flux tube. Subtracting the mean thus retains fluctuations on scales smaller than the east-west extent of the FOV, implying that relative differences in $\partial_\eta\Sigma$ between flux tubes can be measured reliably.

We investigated the flux tube dependence of the field-aligned gradient by binning the data points gathered from all snapshots by ξ value and then computing the average $\partial_\eta\Sigma$ value for each bin. The result is shown in Figure 7, with the characteristic spread within each bin represented by the error bars. There is evidence for systematic variations in $\partial_\eta\Sigma$ on east-west scales of order several tens of kilometers. This is comparable to the observed widths of the FAIs and indicates that plasma scale heights can differ measurably between flux tubes that are several tens of kilometers apart.

To explain the lack of diminished density contrast at high zenith angles, *Loi et al.* [2015a] argued that the thickness of the sheet could not be more than a factor of ∼3 larger than the spacing of the structures. If the thickness is ∼100 km and the background electron density is ∼10^4 el cm^{-3} (characteristic of the nighttime midlatitude topside ionosphere) [*Schunk and Nagy*, 2009], then under the model assumption that all density variations are confined to the screen implies a relative variation in the scale height of ∼100 km between flux tubes within the FOV. Given that absolute scale heights of several hundred kilometers have been measured at similar latitudes, altitudes, and times of day [*Thomas et al.*, 1966; *Watt*, 1966], this appears to be a substantial variation. However, the actual thickness of the screen is largely uncertain, and a thinner screen would yield a proportionally smaller estimate. The physical origin for the local variations in scale height could be temperature differences between flux tubes, perhaps a result of variations in the conductivity tensor combined with storm-related field-aligned currents that produce uneven heating of the plasma, or longitudinally varying rates of impact ionization.

Figure 8. Logarithm of the power spectral density for the (top row) ξ component and (bottom row) η component of the density gradient field $\nabla\Sigma$, collapsed from three dimensions down to two by integrating out ω (left), k_η (middle), and k_ξ (right). Note that these have been zoomed in to the central regions; the absolute Nyquist frequencies are 0.25 km^{-1} for both the k_ξ and k_η axes and 4.2 mHz for the ω axis. The corresponding response function is shown in Figure 9.

4.3. Power Spectra and Wavelike Behavior

This section and the following section present quantitative measurements of the fluctuation properties (wavelengths, periods, and phase velocities) of the $\nabla\Sigma$ vector field using the power spectrum technique developed by *Loi et al.* [2015b]. Spatial coordinates x and y are replaced by ξ and η, and the transformed quantity is $\nabla\Sigma$ (rather than $\nabla_\perp$TEC). We chose a grid size of 2 km, which given a mean sampling density of approximately one pierce point per 100 km^2 on the screen, corresponds to spatially oversampling by a factor of about 2. We computed two power spectra, one for $\partial_\xi\Sigma$ and another for $\partial_\eta\Sigma$. Each is a three-dimensional data cube with two axes for the ξ and η spatial frequencies (denoted by k_ξ and k_η) and one axis for the temporal frequency ω. Figure 8 shows the reduced (from 3-D to 2-D) power spectral density distributions obtained by integrating along each of the axes in turn.

The response function for these power spectra, visualized in an identical manner, is shown in Figure 9. Its compactness assures us that the most of the structure seen in Figure 8, with the exception of the diffuse diagonal band running from top-left to bottom-right in the middle column, is genuine. The band is a typical feature in MWA power spectra and we refer the reader to *Loi et al.* [2015b], section 3.1 for details of its origin.

It can be seen that the greatest concentration of power is in the cells for which $k_\eta = 0$ (Figure 8, left column). This tells us that fluctuations in $\partial_\xi\Sigma$ take the form of corrugations varying almost purely along the ξ direction, which is consistent with Figure 6. As mentioned earlier in section 3.4, the value of i was chosen according to equation (4). This corresponds to choosing the i that concentrates the most signal power into the $k_\eta = 0$ cells. Otherwise put, it is the act of choosing the basis in which as much information is captured in as small a subset
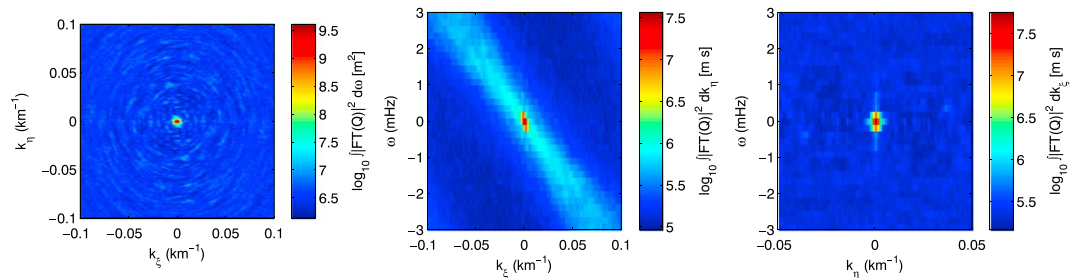

Figure 9. The response function for the power spectra shown in Figure 8. The three panels correspond to integrating out (left) ω, (middle) k_η, and (right) k_ξ. The diagonal ringing feature in Figure 9 (middle) results from the rotation of the Earth and consequent drift motion of measurement points through the screen (see *Loi et al.* [2015b] for a more detailed explanation of its origin).
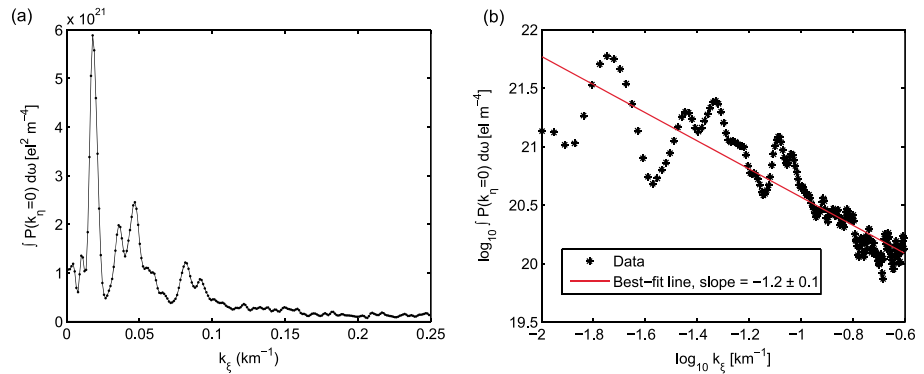
Figure 10. The power spectral density in the $k_\eta = 0$ row of cells from the top-left panel of Figure 8, plotted as a function of k_ξ on (a) linear and (b) logarithmic axes. Since the power spectrum is inversion symmetric, it is only necessary to display one half of the k_ξ axis (we have chosen to plot positive k_ξ). Strong peaks at discrete spatial frequencies can be seen, indicating the presence of distinct modes. A fit to the power spectrum, corresponding to the red line in Figure 10b, suggests that it can globally be described by a power law of index -1.2 ± 0.1.

of basis vectors as possible. The fact that the value of i which achieves this coincides with the magnetic inclination provides the physical interpretation for the structures as FAIs. A separate subsection (section 4.4) is devoted to an analysis of the structure within the $k_\eta = 0$ row of cells.

Comparing Figures 8 (top row) and 8 (bottom row) reveals that peaks tend to be 1–2 orders of magnitude more intense for $\partial_\xi \Sigma$ than $\partial_\eta \Sigma$. It can also be seen from Figures 8 (left column) and 8 (middle column) that the power spectral density for $\partial_\eta \Sigma$ is confined to smaller k_ξ values (larger east-west scales) than $\partial_\xi \Sigma$. This is consistent with Figure 6 and Movie S1.

Phase velocities can be measured from the slopes of features in the ω-k_ξ and ω-k_η planes (middle and right columns). A northeastward propagating fluctuation in $\partial_\eta \Sigma$ can be identified, with a wavelength of ~700 km and a phase speed of about 200 m s^{-1}. This may be an AGW whose presence is revealed only in the $\partial_\eta \Sigma$ component because this component is not overwhelmed by the FAI signal. In contrast, the modes with smaller wavelengths seen in $\partial_\xi \Sigma$ (Figure 8, top row, middle column) are associated with smaller slopes and therefore phase speeds. If one inspects the slopes of lines joining pairs of conjugate peaks one sees that there is a small scatter about $\omega/k_\xi = 0$ m s^{-1}, with some slopes being positive and others negative. This suggests that different modes move with slightly different speeds (typical magnitudes are several meters per second), some drifting east and others west. Since the associated FAIs are likely to be in situ stationary structures, this suggests the presence of east-west shear in the plasma at a rate of ~10 m s^{-1}, which could be a potential source of free energy for growth.

4.4. Spatial Periodicities

The concentration of power into the modes with $k_\eta = 0$ through use of the (ξ, η) basis allows us to isolate this region of the $\partial_\xi \Sigma$ power spectrum for further analysis. The ω-integrated power spectral density distribution as a function of k_ξ for the $k_\eta = 0$ modes is shown in Figure 10. One can identify prominent peaks at distinct spatial frequencies, whose heights roughly decrease with increasing wave number. The corresponding response function, shown in Figure 11, is highly compact and would not be responsible for generating this complex structure.

The most prominent peak is at $k_\xi = 0.018$ km^{-1}, corresponding to a wavelength of 56 km (this periodicity can be visually identified in Figure 6). Additional peaks appear near $k_\xi = 0.036$, 0.047, 0.081, and possibly 0.092 km^{-1}, corresponding to wavelengths of 28, 21, 12, and 11 km, respectively. Note that although the wave number itself can be measured to a precision of 10^{-3} km^{-1} (set by the spatial extent of the observed region), the overall error in these values is dominated by the systematic error arising from the uncertainty in h. This is large, of order 10%, and enters through the role of h in setting the linear scale of the (ξ, η) coordinates with respect to the data, which can be seen from equation (A2).

Although the $k_\eta = 0$ region of the $\partial_\xi \Sigma$ power spectrum has a complicated structure containing multiple peaks, the envelope appears to decay with increasing k_ξ. If we assume a power law functional form, the best fit index turns out to be -1.2 ± 0.1. Note that this applies to the power spectrum of the ξ gradient of Σ. Because the
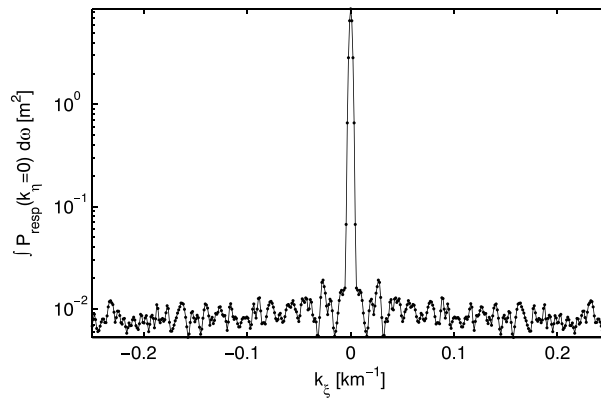
Figure 11. The response function corresponding to the one-dimensional power spectrum shown in Figure 10. Noisy fluctuations have been made visible by the use of a logarithmic scale on the vertical axis. The central peak is about 3 orders of magnitude above the noise and has a width of 3–4 frequency increments.

Fourier transform of the ξ gradient of a function is $-ik_\xi$ times the Fourier transform of the function itself, the power spectrum of $\partial_\xi \Sigma$ is k_ξ^2 times the power spectrum of Σ and so the corresponding index of the *density* power spectrum is -3.2. This may be consistent with the 3-D Kolmogorov index of $-11/3$ [*Kolmogorov*, 1941] to within experimental uncertainty if one acknowledges the possibility of additional sources of error such as spectral leakage, which tends to systematically flatten the spectrum [see *Loi et al.*, 2015b, Appendix A]. Moreover, it is uncertain as to where in wave number space a turbulent cascade might begin. It may be that the peaks seen at $k_\xi < 0.1$ km^{-1} reflect unstable modes where energy is being injected and that the cascade only develops at higher wave numbers. Indeed, the region where $k_\xi > 0.1$ km^{-1} appears to possess a slightly steeper index of -1.4 ± 0.2.

Given the evidence for velocity shear (section 4.3), it is possible that the structures have grown through a Kelvin-Helmholtz instability. The dominant wavelength in this case is around 8 times the width of the shear layer, so if the primary mode is the one at ∼60 km then one infers a thickness for the shearing region of order 10 km. The origin of this shear may be in the neutral atmosphere, or alternatively, the periodicities may reflect those of seed disturbances (e.g., AGWs), where the associated density and conductivity perturbations have mapped upward along field lines to generate the structures observed.
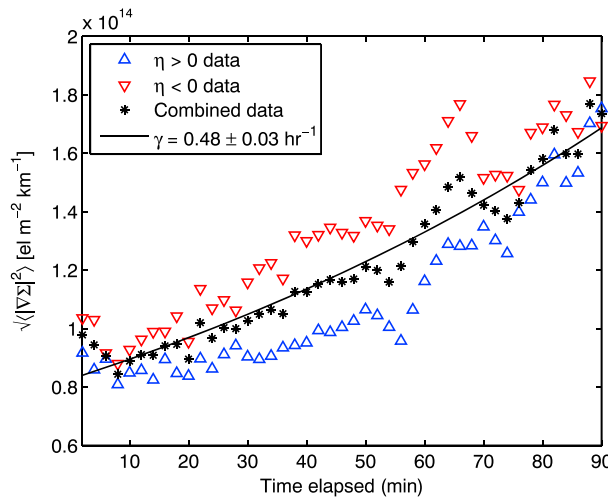

Figure 12. The RMS of density gradients measured through source position offsets and therefore indicating the characteristic amplitude of fluctuations on scales exceeding the size of the MWA (∼1 km), as a function of time. Black asterisks correspond to the RMS value calculated over the whole FOV, whereas the upward pointing (blue) and downward pointing (red) triangles correspond to restrictions to the regions northward ($\eta > 0$) and southward ($\eta < 0$) of zenith, respectively. The slope of the plane toward the north means that this also reflects a split in altitude, with blue triangles being for higher altitudes. The black solid line is an exponential fit ($\propto e^{\gamma t}$) through the asterisks. The best fit value for the growth rate γ corresponds to a timescale of about 2 h.

4.5. Growth Over Observing Interval

As previously noted, the density gradients associated with the FAIs grow over time. This can be quantified by plotting the characteristic $\nabla \Sigma$ value over the FOV as a function of time, shown using black asterisks in Figure 12. To enable a quantitative comparison with the small-scale gradients defined in equation (3) (see later in section 5.2), it is the RMS value of $\nabla \Sigma$ that has been plotted. We obtained the characteristic growth rate γ by fitting to the data an exponential curve (black solid line) of the form $\propto e^{\gamma t}$, where t is time. The best fit growth rate is $\gamma = 0.48 \pm 0.03$ h^{-1}, corresponding to a growth timescale of about 2 h.

We also examined the separate trends for high ($\eta > 0$) and low ($\eta < 0$) altitudes, plotted as the blue and red triangles in Figure 12. While growth on a similar timescale is evident in both regimes, the two curves are noticeably offset with characteristic gradients being about 20% larger at lower altitudes. This could arise if each flux tube were associated
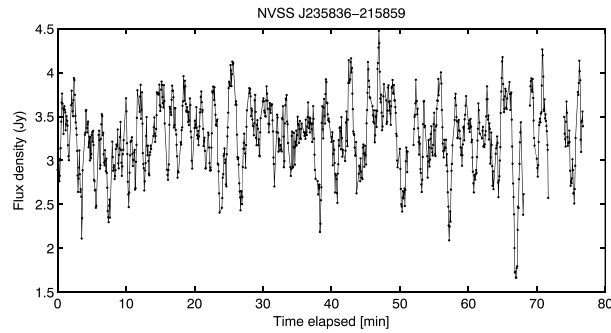
Figure 13. A representative radio light curve (flux density as a function of time) of a randomly selected source, exhibiting a modulation index of order unity on short (tens of seconds) timescales. This is characteristic of diffractive scintillation, evidencing significant structure on subarray scales. Note that this plot was obtained using images formed at a cadence of 4 s. Similar rapidly varying light curves are observed for all other sources in the data set. The error on each flux measurement, given by the local pixel-to-pixel RMS noise, is 0.2 Jy.

with a fixed-percentage fluctuation of the background density; a global decrease in background density with altitude would then explain the separation between the curves.

5. Sub-MWA Structures

5.1. Scintillation

Because an interferometer combines signals coherently, it is susceptible to destructive interference and decorrelation if the phase variation of an incoming signal over the array deviates significantly (by >1 rad) from a linear ramp. This effect is similar to the constructive and destructive interference that results if ray paths are perturbed during propagation to the point where they cross before reaching the detector (cf. Fraunhofer diffraction). The critical size scale of irregularities on which ~1 rad associated phase perturbations cause this to occur (i.e., the Fresnel scale) is around 400 m for the parameters relevant here. These effects give rise to scintillation, where the apparently brightness of the source fluctuates erratically by a significant fraction of the true brightness. The timescale of this fluctuation is given by the spatial scale of the irregularities divided by the drift speed of the sight lines.

Figure 13 shows the radio light curve for a moderately bright (S/N ratio of 15) source in the data. Large modulations, of up to 40% the mean brightness of the source and significantly larger than the uncertainty of the measurement (~0.2 jansky (10^{-26} W m^{-2} Hz^{-1}) (Jy), given by the local pixel-to-pixel noise), can be observed to occur on tens of second timescales. Rapid brightness variations are similarly seen for many other sources in the field and can be interpreted as evidence for substantial phase structure on sub-MWA scales. Although it is in principle possible to attempt a temporal power spectrum analysis of these light curves, this is problematic for several reasons. These include the presence of 8 s data gaps for every 2 min block, abrupt beamformer changes at 30 min intervals, and systematic uncertainties in the direction-dependent instrument gain which contaminate the power spectrum across a wide range of frequencies. Suffice to say that no obvious peaks appear in the temporal power spectra (not shown) that might point to a particular diffractive scale. It is possible that this varies over the FOV, but not much more can be said in this regard.

5.2. Angular Broadening

The quantity $\sigma(\nabla\Sigma)$, defined in equation (3) and representing the characteristic spread in density gradients for FAIs on sub-MWA scales, is plotted as a function of time in Figure 14. We observe that this increases with time and at a similar average rate of growth as for the super-MWA structures. However, the growth curve appears (at least visually) to be segmented into two portions associated with different growth rates, the transition occurring near the 60 min mark. We have chosen to fit these two portions separately and find that the growth rate (given by the slope of the trend) is consistent with undergoing an increase at $t = 60$ min by a factor of $4-5$. The corresponding timescales of growth are $7-8$ h before $t = 60$ min, subsequently dropping to $1-2$ h.

Splitting the data into high ($\eta > 0$) and low ($\eta < 0$) altitude regions reveals another property of the apparent transition at $t = 60$ min. The two growth curves are initially separate, with $\sigma(\nabla\Sigma)$ larger at higher altitudes, but then converge at the transition point (see Figure 14b). The initial difference in $\sigma(\nabla\Sigma)$ between the two regimes could be explained by a larger dissipation rate at lower altitudes, where the environment is more
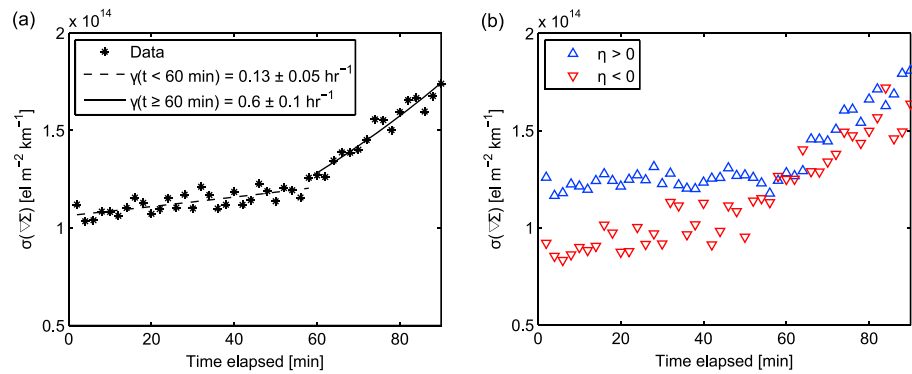
Figure 14. The RMS of density gradients measured through the angular broadening of otherwise unresolved sources, and therefore on scales below the size of the MWA (∼1 km), as a function of time. (a) The trend for sources over the whole field of view. (b) The trend for two sets of sources separated according to whether they lie north (blue) or south (red) of zenith. There appears to be an increase in growth rate near time $t = 60$ min in Figure 14a, which coincides with the time when the two growth curves in Figure 14b, initially separate, converge. To quantify this apparent change in growth rate, the data before and after $t = 60$ min have been fitted separately with exponential functions ($\propto e^{\gamma t}$). These are the dashed and solid lines in Figure 14a, with corresponding best fit growth rates γ indicated in the figure legend.

collisional. The subsequent convergence of the two curves might then be attributed to the increase in growth rate, with the new growth rate being much larger than the difference in dissipation rates between high and low altitudes. Although the situation appears to be reversed compared to super-MWA structures in that higher altitudes are associated with larger gradients, this could be explained by the greater importance of dissipative effects on smaller scales.

It is possible that these small-scale structures derived their energy for formation from the same source as for the larger FAIs. However, large-scale FAIs with density gradients comparable to or greater than this data set have been previously observed by the MWA that were not accompanied by scintillation, which is uncommon at these observing frequencies [*Loi et al.*, 2015c, 2016]. A number of studies that simultaneously monitored the occurrence of VLF whistlers and VHF scintillation have found the two to be uncorrelated, which suggests that large- and small-scale structures may not share the same physical origin [*Singh et al.*, 1994; *Patel et al.*, 2010]. It may be that the simultaneous presence of both large- and small-scale irregularities in this data set is coincidental. However, the observation here that the two share similar growth trends supports the idea that they share a common energy source, so perhaps the small-scale irregularities belong to the high-frequency end of the cascade seen on larger scales (section 4.4). Ascertaining the conditions necessary for simultaneous or independent formation of FAIs of different sizes will require a broader study that is beyond the scope of this work.

It is curious to notice that the value of $\sigma(\nabla\Sigma)$, measuring the power on sub-MWA scales, is very similar to the RMS density gradient for super-MWA scales (compare the vertical axes of Figures 12 and 14), which may be a coincidence. If we can assume that the power law index of -1.2 measured for large-scale density gradient fluctuations can be extrapolated down to small scales (i.e., that these are part of the same spectrum), this gives us a way of estimating the inner scale. Taking the wave numbers associated with the outer scale and MWA to be $k_{out}=10^{-4}$ m^{-1} and $k_{MWA}=10^{-3}$ m^{-1}, and equating the total power (proportional to $\int k^{-1.2}\,dk$) on super- and sub-MWA scales, we obtain $k_{in} \sim 0.1$ m^{-1} for the inner scale. The corresponding length is ∼10 m, comparable to ion gyroradii.

6. Summary and Outlook

We have introduced a new approach for studying FAIs that transforms interferometric TEC gradient data into a physically meaning reference frame, corresponding to the magnetic shell tangent plane. Applying the transformation to the 15 October 2013 data set of *Loi et al.* [2015a], we demonstrated its utility for decomposing behavior along and across magnetic field lines through the construction of a suitable set of coordinates (ξ, η), where the ξ and η directions are perpendicular and parallel to the field, respectively. We also devised a method for computing the best value for the inclination of the plane from the data and verified that it is in good agreement with the magnetic inclination. Through our analyses we found that

1. The transformation to (ξ, η) confirms with much greater precision than previous work that the striations seen by the MWA on 15 October 2013 were oriented along the geomagnetic field;
2. ξ gradients were around an order of magnitude steeper than η gradients and showed structuring on spatial scales of several tens of kilometers, while η gradients were structured on much larger scales of several hundred kilometers;
3. The plasma scale height, quantified through the η gradients, varied by up to ∼100 km between flux tubes within the FOV, possibly reflecting spatial variations in plasma temperature;
4. A differential drift of ∼10 m s^{-1} in the east-west direction could be identified through power spectrum analysis, possibly providing the energy for growth of the FAIs through a shear-driven instability;
5. The spatial power spectrum showed multiple periodicities on scales between 10 and 60 km, which may correspond to those of seed fluctuations (e.g., atmospheric waves) or perhaps the favored wavelengths of a plasma instability;
6. Fitting the power spectrum of ξ gradients with a power law yielded an index of -1.2 ± 0.1, slightly flatter than the Kolmogorov value of $-5/3$;
7. Growth of the FAIs on both large and small spatial scales was observed over the interval, and we measured the characteristic timescales to be several hours;
8. Many background radio sources exhibited strong scintillations, implying significant structure on small (subarray) scales;
9. Angular broadening analyses revealed small-scale irregularities to be highly anisotropic and aligned along the magnetic field;
10. Comparable amounts of fluctuation power were present on large and small scales (relative to the size of the array), allowing us to estimate an inner scale of ∼10 m by extrapolating the power law obtained for large-scale structure; and
11. The strengths of density gradients exhibited an altitude dependence, being greater at lower altitudes for large-scale structure and greater at higher altitudes for small-scale structure, which might be explained through a size-dependent importance of dissipative effects.

The main weakness of our model is the assumption that irregularities are confined to a thin layer. This may be a fair approximation for the interval analyzed here, but there may be periods in which irregularities reside on multiple layers, a situation that would escape detection by the MWA. Because of its small size, the MWA can only perform a crude height localization through parallax analysis to obtain a single characteristic value for the altitude [*Loi et al.*, 2015a]. Interferometers that are more spatially extended, such as the Low Frequency Array [*van Haarlem et al.*, 2013] and the future Square Kilometre Array (SKA) [*Dewdney et al.*, 2009], would be capable of conducting a more detailed three-dimensional mapping of the ionosphere through, e.g., tomographic inversion [*Gaussiran et al.*, 2004; *Koopmans*, 2010].

A convenient property of our model is that it is self-contained: the two input parameters (height and inclination) can be fitted using the data alone. The concepts presented here may pave the way for improvements to ionospheric calibration procedures for next generation radio telescopes. The two-parameter inclined screen model enables most of the FAI fluctuation power to be captured into unidirectional plane wave modes aligned with the Earth's magnetic field. Such a model may be a viable starting point for the development of compact calibration strategies for the SKA, since a relatively small number of basis elements would be needed to represent FAI-related distortions in the data. The ability of interferometers like the MWA to probe ionospheric density structures at great breadth and detail underscores them as rich sources of geophysical information; we hope for their continued application to this end in time to come.

Appendix A: Transformation Equations

Here we present the mathematical details of the transformations applied to the data, namely, the coordinate conversion from astronomical (α, δ) coordinates to the Earth-based (β, γ) coordinates and then the mapping onto the (ξ, η) plane. Since the latter two systems are nonstandard (to our knowledge), their descriptions have been included here for the sake of reproducibility of our work.

The coordinates (α, δ) form a spherical coordinate system whose pole is aligned with the rotation axis of the Earth, α and δ being longitude and latitude, respectively. Zero longitude is defined to pass through the vernal equinox, a point fixed with respect to the stars. Like (α, δ) coordinates, (β, γ) coordinates also form a spherical system, with β and γ being longitude and latitude, respectively. However, the pole of the (β, γ) system is

aligned with geographic east-west, and zero longitude is defined to pass through the zenith. These coordinates are therefore observer dependent, differing from the more familiar Az/El coordinates by a 90° rotation. They are illustrated in Figure 2.

Transforming between (α, δ) and (β, γ) involves a simple rotation operation. To achieve this, one must know two things: the local sidereal time (LST) of the observation and the geographic latitude Λ of the observing location. Defining $\alpha' \equiv \alpha - \text{LST}$, one then computes $\mathbf{x}' = \Phi \mathbf{x}$ where

$$\Phi = \begin{pmatrix} \cos\Lambda & 0 & \sin\Lambda \\ -\sin\Lambda & 0 & \cos\Lambda \\ 0 & -1 & 0 \end{pmatrix}, \quad \mathbf{x} = \begin{pmatrix} \cos\delta\cos\alpha' \\ \cos\delta\sin\alpha' \\ \sin\delta \end{pmatrix} \tag{A1}$$

and inverts $\mathbf{x}' = (\cos\gamma\cos\beta, \cos\gamma\sin\beta, \sin\gamma)$ for β and γ. At the MWA site, $\Lambda = -26.7°$. One can see that the transformation operation is time dependent, reflecting the fact that the two coordinate systems move with respect to one another (since the Earth rotates with respect to the stars).

Given that the conversion from (α, δ) to (β, γ) is nothing more than a basis transformation, the (β, γ) representation of a $\nabla_\perp\text{TEC}$ vector given its (α, γ) representation can be obtained by applying the above operations to the endpoints of the corresponding angular offset vectors. That is, if a source whose true position lies at (α_0, δ_0) is observed to be displaced by $(\Delta\alpha, \Delta\delta)$, then we would use the mapping described above to take $(\alpha_0, \delta_0) \rightarrow (\beta_0, \gamma_0)$ and $(\alpha_0 + \Delta\alpha, \delta_0 + \Delta\delta) \rightarrow (\beta_1, \gamma_1)$. Then $\nabla_\perp\text{TEC} = (\partial_\beta\text{TEC}, \partial_\gamma\text{TEC})$ can be obtained by substituting $\Delta\theta = ([\beta_1 - \beta_0]\cos\gamma_0, \gamma_1 - \gamma_0)$ into equation (1).

Next, we specify how to obtain $\xi, \eta, \partial_\xi\Sigma$, and $\partial_\eta\Sigma$ from $\beta, \gamma, \partial_\beta\text{TEC}$, and $\partial_\gamma\text{TEC}$. Unlike the transformation from (α, δ) to (β, γ), this is not merely a change of basis but a mapping between different vectors in 3-D space. The geometrical setup is illustrated in Figure 2. Once h and i are chosen, (ξ, η) can be found by projecting (β, γ) onto the screen:

$$\begin{pmatrix} \xi \\ \eta \end{pmatrix} = \frac{h}{\cos(\beta + i)} \begin{pmatrix} \cos i \tan\gamma \\ \sin\beta \end{pmatrix}. \tag{A2}$$

Finding $\partial_\xi\Sigma$ and $\partial_\eta\Sigma$ requires a more involved sequence of operations. It is *not* correct to simply project the endpoints of an angular displacement vector onto the screen and take the resulting separation to represent $\nabla\Sigma$, because equation (1) no longer applies. To understand how $\nabla_\perp\text{TEC}$ should map to $\nabla\Sigma$, observe that the local gradient vector of any scalar field defined on a surface measured from a certain vantage point is inversely proportional to the apparent distance between two contours (i.e., lines joining points of equal value). Since the spacing between two given contours on a surface is foreshortened by the cosine of the angle at which the surface is viewed, the corresponding gradient vector will be *forelengthened* by this factor. If we denote the normal vector to the surface by $\hat{\mathbf{n}}$, this means that $\nabla_\perp\text{TEC}$ must be elongated by a factor $|\hat{\mathbf{n}} \cdot \mathbf{x}'|$ along the viewing direction. For our simple 2-D plane model, $\hat{\mathbf{n}} = (-\cos i, \sin i, 0)$. We obtained (after some algebra) the following expressions for the components of $\nabla\Sigma$:

$$\partial_\xi\Sigma = \sin\gamma\cos\gamma\sin(\beta + i)\cos(\beta + i) \times [\cos i\cos\gamma\cos(\beta + i) + \sin i - 1]\partial_\beta\text{TEC}$$
$$+ \left\{\sin^2\gamma\cos\gamma\cos^2(\beta + i)[\cos i\cos(\beta + i) + \sin i] + \cos\gamma\sin^2(\beta + i)\right\}\partial_\gamma\text{TEC} \tag{A3}$$

$$\partial_\eta\Sigma = \cos(\beta + i)\left\{\sin^2(\beta + i)\cos^2\gamma \times [\cos(\beta + i)\cos\gamma\cos i + \sin i] + \sin^2\gamma\right\}\partial_\beta\text{TEC}$$
$$+ \sin(\beta + i)\sin\gamma\left\{\cos^2(\beta + i)\cos^2\gamma \times [\cos(\beta + i)\cos i\cos\gamma + \sin i] - 1\right\}\partial_\gamma\text{TEC}. \tag{A4}$$

Equations (A3) and (A4) are the equations used in the current work. For a more sophisticated model that deals with curvature effects, such as a dipole shell model, it is not necessarily the case that convenient closed-form expressions can be found. In the case of a dipole, $\hat{\mathbf{n}}$ is a function of ξ, and obtaining ξ itself requires as an intermediate step solving a quintic in the radius of the dipole shell at the pierce point. This would be possible in practice through numerical means. However, the planar model appeals at the present stage because of its simplicity and compactness of implementation. Alternative or more refined models could be considered in future extensions to this work.

A useful generalization of the planar model would be to allow for a nonzero magnetic declination D (as implemented, the equations in fact align $\hat{\eta}$ with geographic east-west). This could be achieved by introducing an

alternative definition for the (β, γ) coordinate system, where the pole is aligned with geomagnetic rather than geographic east-west. In this situation, Φ would be replaced by the more general matrix

$$\Phi' = \begin{pmatrix} \cos\Lambda & 0 & \sin\Lambda \\ -\sin\Lambda\sin D' & \cos D' & \cos\Lambda\sin D' \\ -\sin\Lambda\cos D' & -\sin D' & \cos\Lambda\cos D' \end{pmatrix},$$

(A5)

where $D' \equiv 90° - D$. See that this reduces to Φ in equation (A1) when $D = 0°$. At the location of the MWA, D is around $-0.2°$ [*Geoscience Australia*, 2010] and so has been neglected. However, similar analyses of data taken at locations where the magnetic declination is substantial (in excess of a few degrees) should use equation (A5) rather than equation (A1) if the form of equations (A2)–(A4) is to be preserved.

References

Akmaev, R. A. (2011), Whole atmosphere modeling: Connecting terrestrial and space weather, *Rev. Geophys.*, *49*, RG4004, doi:10.1029/2011RG000364.

Altaf, M., and M. M. Ahmad (2013), Study of duct characteristics deduced from low latitude ground observations of day-time whistler at Jammu, *Int. J. Astron. Astrophys.*, *3*, 274–277, doi:10.4236/ijaa.2013.33032.

Angerami, J. J. (1970), Whistler duct properties deduced from VLF observations made with the OGO 3 satellite near the magnetic equator, *J. Geophys. Res.*, *75*(31), 6115–6135, doi:10.1029/JA075i031p06115.

Arora, B. S., et al. (2015), Ionospheric modelling using GPS to calibrate the MWA. I: Comparison of first order ionospheric effects between GPS models and MWA observations, *Publ. Astron. Soc. Aust.*, *32*, e029, doi:10.1017/pasa.2015.29.

Booker, H. G. (1979), The role of acoustic gravity waves in the generation of spread-F and ionospheric scintillation, *J. Atmos. Terr. Phys.*, *41*, 501–515, doi:10.1016/0021-9169(79)90074-6.

Booker, H. G., and G. Majidiahi (1981), Theory of refractive scattering in scintillation phenomena, *J. Atmos. Terr. Phys.*, *43*(11), 1199–1214, doi:10.1016/0021-9169(81)90035-0.

Booker, J. R., and F. P. Bretherton (1967), The critical layer for internal gravity waves in a shear flow, *J. Fluid Mech.*, *27*(3), 513–539, doi:10.1017/S0022112067000515.

Bougeret, J. L. (1981), Some effects produced by the ionosphere on radio interferometry: Fluctuations in apparent source position and image distortion, *Astron. Astrophys.*, *96*, 259–266.

Bowman, J. D., et al. (2013), Science with the Murchison Widefield Array, *Publ. Astron. Soc. Aust.*, *30*(2013), e31, doi:10.1017/pas.2013.009.

Calvert, W. (1995), Wave ducting in different wave modes, *J. Geophys. Res.*, *100*(A9), 17,491–17,497, doi:10.1029/95JA01131.

Calvert, W., and J. M. Warnock (1969), Ionospheric irregularities observed by topside sounders, *Proc. IEEE*, *57*, 1019–1025, doi:10.1109/PROC.1969.7146.

Carpenter, D. L., and R. L. Smith (1964), Whistler measurements of electron density in the magnetosphere, *Rev. Geophys.*, *2*(3), 415–441, doi:10.1029/RG002i003p00415.

Carter, B. A., E. Yizengaw, J. M. Retterer, M. Francis, M. Terkildsen, R. Marshall, R. Norman, and K. Zhang (2014), An analysis of the quiet time day-to-day variability in the formation of postsunset equatorial plasma, *J. Geophys. Res. Space Physics*, *119*, 3206–223, doi:10.1002/2013JA019570.

Cohen, A. S., and H. J. A. Röttgering (2009), Probing fine-scale ionospheric structure with the Very Large Array radio telescope, *Astrophys. J.*, *138*(2), 439–447, doi:10.1088/0004-6256/138/2/439.

Coker, C., S. E. Thonnard, K. F. Dymond, T. J. W. Lazio, J. J. Makela, and P. J. Loughmiller (2009), Simultaneous radio interferometer and optical observations of ionospheric structure at the Very Large Array, *Radio Sci.*, *44*, RS0A11, doi:10.1029/2008RS004079.

Condon, J. J., W. D. Cotton, E. W. Greisen, Q. F. Yin, R. A. Perley, G. B. Taylor, and J. J. Broderick (1998), The NRAO VLA Sky Survey, *Astrophys. J.*, *115*, 1693, doi:10.1086/300337.

Cotton, W. D., J. J. Condon, R. A. Perley, N. Kassim, J. Lazio, A. Cohen, W. Lane, and W. C. Erickson (2004), Beyond the isoplanatic patch in the VLA Low-Frequency Sky Survey, *Proc. SPIE*, *5489*, 180–189, doi:10.1117/12.551298.

Darrouzet, F., et al. (2009), Plasmaspheric density structures and dynamics: Properties observed by the CLUSTER and IMAGE missions, *Space Sci. Rev.*, *145*(1–2), 55–106, doi:10.1007/s11214-008-9438-9.

Décréau, P. M. E., E. Le Guirriec, J. L. Rauch, J. G. Trotignon, P. Canu, F. Darrouzet, J. Lemaire, a. Masson, F. Sedgemore, and M. André (2005), Density irregularities in the plasmasphere boundary player: CLUSTER observations in the dusk sector, *Adv. Space Res.*, *36*(10), 1964–1969, doi:10.1016/j.asr.2005.08.050.

Dewdney, P. E., P. J. Hall, R. T. Schilizzi, and T. J. L. W. Lazio (2009), The square kilometre array, *Proc. IEEE*, *97*(8), 1482–1496, doi:10.1109/JPROC.2009.2021005.

Dyson, P. L. (1967), Magnetic field-aligned irregularities at mid-geomagnetic latitudes, *J. Atmos. Terr. Phys.*, *29*, 857–869, doi:10.1016/0021-9169(67)90051-7.

Dyson, P. L., and R. F. Benson (1978), Topside sounder observations of equatorial bubbles, *Geophys. Res. Lett.*, *5*(9), 795–798, doi:10.1029/GL005i009p00795.

Farley, D. T., Jr. (1963), A plasma instability resulting in field-aligned irregularities in the ionosphere, *J. Geophys. Res.*, *68*(22), 6083–6097, doi:10.1029/JZ068i022p06083.

Fejer, B. G., and M. C. Kelley (1980), Ionospheric irregularities, *Rev. Geophys. Space Phys.*, *18*(2), 401–454, doi:10.1029/RG018i002p00401.

Fejer, B. G., L. Scherliess, and E. R. de Paula (1999), Effects of the vertical plasma drift velocity on the generation and evolution of equatorial spread F, *J. Geophys. Res.*, *104*(A9), 19,859–19,869, doi:10.1029/1999JA900271.

Fritts, D. C., and S. L. Vadas (2008), Gravity wave penetration into the thermosphere: Sensitivity to solar cycle variations and mean winds, *Ann. Geophys.*, *26*(1988), 3841–3861, doi:10.5194/angeo-26-3841-2008.

Fung, S. F., and J. L. Green (2005), Modeling of field-aligned guided echoes in the plasmasphere, *J. Geophys. Res.*, *110*, A01210, doi:10.1029/2004JA010658.

Fung, S. F., R. F. Benson, D. L. Carpenter, W. Bodo, and D. L. Gallagher (2000), Investigations of irregularities in remote plasma regions by radio sounding: Applications of the Radio Plasma Imager on IMAGE, *Space Sci. Rev.*, *91*, 391–419.

Fung, S. F., R. F. Benson, D. L. Carpenter, J. L. Green, V. Jayanti, I. A. Galkin, and B. W. Reinisch (2003), Guided echoes in the magnetosphere: Observations by Radio Plasma Imager on IMAGE, *Geophys. Res. Lett.*, *30*(11), 1589, doi:10.1029/2002GL016531.

Gaussiran, T. L., II, G. S. Bust, and T. W. Garner (2004), LOFAR as an ionospheric probe, *Planet. Scape Sci.*, *52*(15), 1375–1380, doi:10.1016/j.pss.2004.09.007.

Geoscience Australia (2010), Australian Geomagnetic Field Reference Values, Geoscience Australia. [Available at http://www.ga.gov.au/metadata-gateway/metadata/record/71108/.]

Gross, S. H., and D. B. Muldrew (1984), Uniformly spaced field-aligned ionization ducts, *J. Geophys. Res.*, *89*(A10), 8986–8996, doi:10.1029/JA089iA10p08986.

Hamaker, J. P. (1978), Atmospheric delay fluctuations with scale sizes greater than one kilometer, observed with a radio interferometer array, *Radio Sci.*, *13*(5), 873–891, doi:10.1029/RS013i005p00873.

Hancock, P. J., T. Murphy, B. M. Gaensler, A. Hopkins, and J. R. Curran (2012), Compact continuum source finding for next generation radio surveys, *Mon. Not. R. Astron. Soc.*, *422*(2), 1812–1824, doi:10.1111/j.1365-2966.2012.20768.x.

Haselgrove, J. (1955), Ray theory and a new method for ray tracing, in *London Physical Society Report of Conference on the Physics of the Ionosphere*, pp. 355–364, Phys. Soc., London.

Hayakawa, M., and Y. Tanaka (1978), On the propagation of low-latitude whistlers, *Rev. Geophys. Space Phys.*, *16*(7), 111–122, doi:10.1029/RG016i001p00111.

Helmboldt, J. F. (2014), Drift-scan imaging of traveling ionospheric disturbances with the Very Large Array, *Geophys. Res. Lett.*, *41*, 4835–4843, doi:10.1002/2014GL060951.

Helmboldt, J. F., and H. T. Intema (2012), Very Large Array observations of disturbed ion flow from the plasmasphere to the nighttime ionosphere, *Radio Sci.*, *47*, RS0K03, doi:10.1029/2012RS004979.

Helmboldt, J. F., W. M. Lane, and W. D. Cotton (2012a), Climatology of midlatitude ionospheric disturbances from the Very Large Array Low-Frequency Sky Survey, *Radio Sci.*, *47*, RS5008, doi:10.1029/2012RS005025.

Helmboldt, J. F., T. J. W. Lazio, H. T. Intema, and K. F. Dymond (2012b), A new technique for spectral analysis of ionospheric TEC fluctuations observed with the Very Large Array VHF system: From QP echoes to MSTIDs, *Radio Sci.*, *47*, RS0L02, doi:10.1029/2011RS004787.

Hoogeveen, G. W., and A. R. Jacobson (1997a), Improved analysis of plasmasphere motion using the VLA radio interferometer, *Ann. Geophys.*, *15*, 236–245, doi:10.1007/s00585-997-0236-6.

Hoogeveen, G. W., and A. R. Jacobson (1997b), Radio interferometer measurements of plasmasphere density structures during geomagnetic storms, *J. Geophys. Res.*, *102*(A7), 14,177–14,188, doi:10.1029/97JA00484.

Intema, H. T., S. van der Tol, W. D. Cotton, A. S. Cohen, I. M. van Bemmel, and H. J. A. Röttgering (2009), Ionospheric calibration of low frequency radio interferometric observations using the peeling scheme I. Method description and first results, *Astron. Astrophys.*, *501*(3), 1185–1205, doi:10.1051/0004-6361/200811094.

Jacchia, L. G. (1977), Thermospheric temperature, density, and composition: New models, *SAO Spec. Rep. 375*, 1–97, Smithsonian Astrophys. Obs., Cambridge, Mass.

Jacobson, A. R., and W. C. Erickson (1992a), A method for characterizing transient ionospheric disturbances using a large radiotelescope array, *Astron. Astrophys.*, *257*, 401–409.

Jacobson, A. R., and W. C. Erickson (1992b), Wavenumber-resolved observations of ionospheric waves using the Very Large Array radiotelescope, *Planet. Space Sci.*, *40*(4), 447–455, doi:10.1016/0032-0633(92)90163-l.

Jacobson, A. R., and W. C. Erickson (1993), Observations of electron density irregularities in the plasmasphere using the VLA radio interferometer, *Ann. Geophys.*, *11*(10), 869–888.

Jacobson, A. R., G. Hoogeveen, R. C. Carlos, and M. C. Kelley (1996), Observations of inner plasmasphere irregularities with a satellite-beacon radio-interferometer array, *J. Geophys. Res.*, *101*(A9), 19,665–19,682, doi:10.1029/96JA01253.

Kassim, N. E., T. J. W. Lazio, W. C. Erickson, R. A. Perley, W. D. Cotton, E. W. Greisen, A. S. Cohen, B. Hicks, H. R. Schmitt, and D. Katz (2007), The 74 MHz system on the Very Large Array, *Astrophys. J. Suppl. Ser.*, *172*(2), 686–719, doi:10.1086/519022.

Kazimirovsky, E., M. Herraiz, and B. A. de la Morena (2003), Effects on the ionosphere due to phenomena occurring below it, *Surv. Geophys.*, *24*, 139–184, doi:10.1023/A:1023206426746.

Klostermeyer, J. (1978), Nonlinear investigation of the spatial resonance effect in the nighttime equatorial F region, *J. Geophys. Res.*, *83*(8), 3753–3760, doi:10.1029/JA083iA08p03753.

Kolmogorov, A. N. (1941), The local structure of turbulence in incompressible viscous fluid for very large Reynolds numbers, *Dokl. Akad. Nauk SSSR*, *30*(4), 301–304.

Koopmans, L. V. E. (2010), Ionospheric power-spectrum tomography in radio interferometry, *Astrophys. J.*, *718*(2), 963–971, doi:10.1088/0004-637X/718/2/963.

Kulkarni, P., U. S. Inan, T. F. Bell, and J. Bortnik (2008), Precipitation signatures of ground-based VLF transmitters, *J. Geophys. Res.*, *113*, A07214, doi:10.1029/2007JA012569.

Lichtenberger, J. (2009), A new whistler inversion method, *J. Geophys. Res.*, *114*, A07222, doi:10.1029/2008JA013799.

Lichtenberger, J., et al. (2013), The plasmasphere during a space weather event: First results from the PLASMON project, *J. Space Weather Space Clim.*, *3*, A23, doi:10.1051/swsc/2013045.

Loi, S. T., et al. (2015a), Real-time imaging of density ducts between the plasmasphere and ionosphere, *Geophys. Res. Lett.*, *42*, 3707–3714, doi:10.1002/2015GL063699.

Loi, S. T., et al. (2015b), Power spectrum analysis of ionospheric fluctuations with the Murchison Widefield Array, *Radio Sci.*, *50*, 574–597, doi:10.1002/2015RS005711.

Loi, S. T., et al. (2015c), Quantifying ionospheric effects on time-domain astrophysics with the Murchison Widefield Array, *Mon. Not. R. Astron. Soc.*, *453*(3), 2731–2746, doi:10.1093/mnras/stv1808.

Loi, S. T., et al. (2016), Density duct formation in the wake of a travelling ionospheric disturbance: Murchison Widefield Array observations, *J. Geophys. Res. Space Physics*, *121*, 1569–1586, doi:10.1002/2015JA022052.

Lonsdale, C. J. (2005), Configuration considerations for low frequency arrays, in *From Clark Lake to the Long Wavelength Array: Bill Erickson's Radio Science, ASP Conf. Ser.*, vol. 345, edited by N. Kassim et al., pp. 399–409, Astron. Soc. of the Pac., San Francisco, Calif.

Lonsdale, C. J., et al. (2009), The Murchison Widefield Array: Design overview, *Proc. IEEE*, *97*(8), 1497–1506, doi:10.1109/JPROC.2009.2017564.

Makela, J. J., and Y. Otsuka (2012), Overview of nighttime ionospheric instabilities at low- and mid-latitudes: Coupling aspects resulting in structuring at the mesoscale, *Space Sci. Rev.*, *168*(1–4), 419–440, doi:10.1007/s11214-011-9816-6.

Maruyama, T. (1990), $E \times B$ instability in the F-region at low- to midlatitudes, *Planet. Space Sci.*, *38*(2), 273–285, doi:10.1016/0032-0633(90)90092-5.

McIlwain, C. E. (1961), Coordinates for mapping the distribution of magnetically trapped particles, *J. Geophys. Res.*, *66*(11), 3681–3691, doi:10.1029/JZ066i011p03681.

Menk, F. W., D. Orr, M. A. Clilverd, a. J. Smith, C. L. Waters, D. K. Milling, and B. J. Fraser (1999), Monitoring spatial and temporal variations in the dayside plasmasphere using geomagnetic field line resonances, *J. Geophys. Res.*, *19*(A9), 19,955–19,969, doi:10.1029/1999JA900205.

Menk, F. W., C. L. Waters, and I. S. Dunlop (2007), ULF Doppler oscillations in the low latitude ionosphere, *Geophys. Res. Lett.*, *34*, L10104, doi:10.1029/2007GL029300.

Mercier, C. (1986), Observations of atmospheric gravity waves by radiointerferometry, *J. Atmos. Terr. Phys.*, *48*(7), 605–624, doi:10.1016/0021-9169(86)90010-3.

Meyer-Vernet, N. (1980), On a day-time ionospheric effect on some radio intensity measurements and interferometry, *Astron. Astrophys.*, *84*, 142–147.

Muldrew, D. (1963), Radio propagation along magnetic field-aligned sheets of ionization observed by the Alouette topside sounder, *J. Geophys. Res.*, *68*(19), 5355–5370.

Nicolls, M. J., and M. C. Kelley (2005), Strong evidence for gravity wave seeding of an ionospheric plasma instability, *Geophys. Res. Lett.*, *32*, L05108, doi:10.1029/2004GL020737.

Nicolls, M. J., S. L. Vadas, N. Aponte, and M. P. Sulzer (2014), Horizontal parameters of daytime thermospheric gravity waves and E region neutral winds over Puerto Rico, *J. Geophys. Res. Space Physics*, *119*, 575–600, doi:10.1002/2013JA018988.

Ossakow, S. L. (1981), Spread-F theories—A review, *J. Atmos. Terr. Phys.*, *43*(516), 437–452, doi:10.1016/0021-9169(81)90107-0.

Park, C. G., and R. A. Helliwell (1971), The formation by electric fields of field-aligned irregularities in the magnetosphere, *Radio Sci.*, *6*(2), 299–304, doi:10.1029/RS006i002p00299.

Patel, R. P., K. Patel, A. K. Singh, and R. P. Singh (2010), Simultaneous observation of VLF and VHF wave in the presence of ionospheric irregularities, *J. Indian Geophys. Union*, *14*(2), 139–148.

Perkins, F. (1973), Spread F and ionospheric currents, *J. Geophys. Res.*, *78*(1), 218–226, doi:10.1029/JA078i001p00218.

Platt, I., and P. Dyson (1989), MF and HF propagation characteristics of ionospheric ducts, *J. Atmos. Terr. Phys.*, *51*, 759–774, doi:10.1016/0021-9169(89)90033-0.

Poole, A. W. V., P. R. Sutcliffe, and A. D. M. Walker (1988), The relationship between ULF geomagnetic pulsations and ionospheric Doppler oscillations: Derivation of a model, *J. Geophys. Res.*, *93*(A12), 14,656–14,664, doi:10.1029/JA093iA12p14656.

Schunk, R. W., and A. F. Nagy (2009), *Ionospheres: Physics, Plasma Physics and Chemistry*, 2nd ed., Cambridge Univ. Press, Cambridge, U. K.

Singh, A. K., and R. P. Singh (1999), Duct lifetimes at mid latitudes, *Period. Polytech. Ser. El. Eng.*, *43*(1), 43–52.

Singh, K. K., S. A. Sheikh, A. K. Singh, and F. Ahmad (2013), Estimation of duct-lifetimes for storm-time low latitude whistlers observed at Srinagar, India, *Indian J. Phys.*, *87*(6), 499–505, doi:10.1007/s12648-013-0274-8.

Singh, R. P., A. K. Singh, U. P. Singh, and R. N. Singh (1994), Wave ducting and scattering properties of ionospheric irregularities, *Adv. Space Res.*, *14*(9), 225–228, doi:10.1016/0273-1177(94)90140-6.

Singh, R. P., A. K. Singh, and D. K. Singh (1998), Plasmaspheric parameters as determined from whistler spectrograms: A review, *J. Atmos. Sol. Terr. Phys.*, *60*(5), 495–508, doi:10.1016/S1364-6826(98)00001-7.

Smith, R. L. (1961), Propagation characteristics of whistlers trapped in field-aligned columns of enhanced ionization, *J. Geophys. Res.*, *66*(11), 3699–3707, doi:10.1029/JZ066i011p03699.

Smith, R. L., R. A. Helliwell, and I. W. Yabroff (1960), A theory of trapping of whistlers in field-aligned columns of ionization, *J. Geophys. Res.*, *65*(3), 815–823, doi:10.1029/JZ065i003p00815.

Sojka, J. J., M. V. Subramanium, L. Zhu, and R. W. Schunk (1998), Gradient drift instability growth rates from global-scale modeling of the polar ionosphere, *Radio Sci.*, *33*(6), 1915–1928, doi:10.1029/98RS02490.

Sonwalkar, V. S. (2006), The influence of plasma density irregularities on whistler-mode wave propagation, in *Geospace Electromagnetic Waves and Radiation*, vol. 191, edited by J. W. LaBelle and R. A. Treumann, pp. 141–190, Springer, Berlin, doi:10.1007/3-540-33203-0_6.

Sonwalkar, V. S., U. S. Inan, T. F. Bell, R. A Helliwell, V. M. Chmyrev, Y. P. Sobolev, O. Y. Ovcharenko, and V. Selegej (1994), Simultaneous observations of VLF ground transmitter signals on the DE 1 and COSMOS 1809 satellites: Detection of a magnetospheric caustic and a duct, *J. Geophys. Res.*, *99*(A9), 17,511–17,522, doi:10.1029/94JA00866.

Spoelstra, T. A. T. (1985), Effects of amplitude and phase scintillations on decimeter wavelength observations at mid-latitudes, *Astron. Astrophys.*, *148*, 21–28.

Spoelstra, T. A. T. (1997), The ionosphere and radio interferometry, *Ann. Geophys.*, *15*(4), 865–885, doi:10.4401/ag-3885.

Spoelstra, T. A. T., and H. Kelder (1984), Effects produced by the ionosphere on radio interferometry, *Radio Sci.*, *19*(3), 779–788, doi:10.1029/RS019i003p00779.

Staquet, C., and J. Sommeria (2002), Internal gravity waves: From instabilities to turbulence, *Annu. Rev. Fluid Mech.*, *34*(1), 559–593, doi:10.1146/annurev.fluid.34.090601.130953.

Storey, L. R. O. (1953), An investigation of whistling atmospherics, *Philos. Trans. R. Soc. A*, *246*(908), 113–141, doi:10.1098/rsta.1953.0011.

Sun, L., J. Xu, W. Wang, X. Yue, W. Yuan, B. Ning, D. Zhang, and F. C. de Meneses (2015), Mesoscale field-aligned irregularity structures (FAIs) of airglow associated with medium-scale traveling ionospheric disturbances (MSTIDs), *J. Geophys. Res. Space Physics*, *120*, 9839–9858, doi:10.1002/2014JA020944.

Thomas, J. O., M. J. Rycroft, and L. Colin (1966), Electron densities and scale heights in the topside ionosphere: Alouette I observations in midlatitudes, *Tech. Rep.*, Sci. and Tech. Inf. Div., NASA, Washington, D. C.

Thompson, A. R., J. M. Moran, and G. W. Swenson Jr. (2001), *Interferometry and Synthesis in Radio Astronomy*, 2nd ed., John Wiley, Weinheim, Germany.

Thomson, R. J. (1978), The formation and lifetime of whistler ducts, *Planet. Space Sci.*, *26*, 423–430, doi:10.1016/0032-0633(78)90064-8.

Tingay, S. J., et al. (2013), The Murchison Widefield Array: The Square Kilometre Array precursor at low radio frequencies, *Publ. Astron. Soc. Aust.*, *30*, e007, doi:10.1017/pasa.2012.007.

Tu, J., P. Song, B. W. Reinisch, J. L. Green, and X. Huang (2006), Empirical specification of field-aligned plasma density profiles for plasmasphere refilling, *J. Geophys. Res.*, *111*, A06216, doi:10.1029/2005JA011582.

van Haarlem, M. P., et al. (2013), LOFAR: The low-frequency array, *Astron. Astrophys.*, *556*, A2, doi:10.1051/0004-6361/201220873.

van Velthoven, P. F. J. (1990), Medium scale irregularities in the ionospheric electron content, PhD thesis, Eindhoven Univ. of Tech., Eindhoven, Netherlands.

van Weeren, R. J., et al. (2016), LOFAR facet calibration, *Astrophys. J. Suppl. Ser.*, *223*, 16, doi:10.3847/0067-0049/223/1/2.

Wang, C. Y., Y. H. Chu, C. L. Su, R. M. Kuong, H. C. Chen, and K. F. Yang (2011), Statistical investigations of layer-type and clump-type plasma structures of 3-m field-aligned irregularities in nighttime sporadic e region made with Chung-Li VHF radar, *J. Geophys. Res.*, *116*, A12311, doi:10.1029/2011JA016696.

Waters, C. L., and S. P. Cox (2009), ULF wave effects on high frequency signal propagation through the ionosphere, *Ann. Geophys.*, *27*, 2779–2788, doi:10.5194/angeo-27-2779-2009.

Watt, T. M. (1966), Correlation of plasma scale height with Kp in the topside ionosphere, *J. Geopghys. Res.*, *71*(13), 3131–3140, doi:10.1029/JZ071i013p03131.

Whitehead, J. D. (1971), Ionization disturbances caused by gravity waves in the presence of an electrostatic field and background wind, *J. Geopghys. Res.*, *76*(1), 238–241, doi:10.1029/JA076i001p00238.

Woodroffe, J. R., A. V. Streltsov, A. Vartanyan, and G. M. Milikh (2013), Whistler propagation in ionospheric density ducts: Simulations and DEMETER observations, *J. Geophys. Res. Space Physics*, *118*, 7011–7018, doi:10.1002/2013JA019445.

Yeh, K. C., and C. H. Liu (1974), Acoustic-gravity waves in the upper atmosphere, *Rev. Geophys. Space Phys.*, *12*(2), 193–216, doi:10.1029/RG012i002p00193.